

PAH band ratios across a variety of environments in the Magellanic Clouds [★]

S. Hony¹, Frederic, Sue, Ciska, Ji-yeon, Naslim, Vianney, Karl, Remy, and Others

¹ ITA

e-mail: sacha.hony@free.fr

² Institute2

XXX;XXX

ABSTRACT

Context. Polycyclic aromatic hydrocarbon (PAHs) emission bands in the mid-IR are key tracers used to diagnose the physical and chemical conditions in a wide range of astrophysical environments. The specific PAH bands in the mid-IR are known to vary in relative strength, indicative of these varying conditions.

Aims. To measure the PAH band-ratios across a large number of lines of sight (\sim XXX) in the Magellanic Cloud galaxies at the smallest attainable spatial scales.

Methods. We use *Spitzer*/IRS low spectral resolution large mapping observations across 12 regions obtained by SAGE-SPEC and S⁴MC. We optimize the spatial resolution by concentrating on the 5–14 μ m range(SL2,SL3 and SL1 orders) which contains the main PAH features are 6.2, 7.7, 8.6, 11.2 and 12.7 μ m.

Results. We find that: 1) The observed ratios span a range of \sim 3 in both galaxies. 2) The predominant band-ratio variations are compatible with changes in the PAH ionisation state. 3) The lowest 7.7/11.2 band ratios are often found along the fainter lines-of-sight and as a consequence averaging over larger beams will increase the observed band ratio. 4) We find for first time a positive correlation between band ratios and 10/100 continuum.

1. Introduction

Emission from polycyclic aromatic hydrocarbons (PAHs) in interstellar environments is ubiquitous and widely used as a tracer for star formation activity. The energetic ultraviolet radiation from newly formed stars excites PAH molecules which then reradiate this energy at mid-infrared wavelengths in a number of discrete spectral features. Prominent features are observed at 3.3, 6.2, 7.7,

[★] This work is based on observations made with the Spitzer Space Telescope, which is operated by the Jet Propulsion Laboratory, California Institute of Technology under a contract with NASA. Support for this work was provided by NASA.

8.6, 11.2, 12.7 and 16.4 μm (see Tielens 2008, and references therein), where each of these resonances can be ascribed to a different vibrational mode in the population of PAH molecules. The shape of the features depends on the combination of chemical compositions and molecular structures within the population of PAH molecules responsible for those features. Peeters et al. (2002) observationally classify PAHs in three different groups (A, B and C), showing very different spectral appearances for the resonances that give rise to the mid-infrared features.

Identification of the modes that are responsible for the mid-infrared features has allowed for a new field of research to open up: the use of PAH band ratios as a diagnostic tool. For instance, Hony et al. (2001) demonstrate that the ratio between the 11.2 and 12.7 μm out-of-plane bending mode band strengths is a measure for the compactness of PAHs. Sources with high values of 11.2/12.7 have a high abundance of compact PAHs, while with decreasing 11.2/12.7 the PAHs are becoming more open, a process thought to be due to erosion or degradation in a radiation field. Other examples include the 6.2/11.2 and 7.7/11.2 ratios, which represents the ratio between CC and CH modes in the PAH molecules. This ratio is sensitive to radiation field which ionizes the PAHs, with a higher degree of ionization seen as an increase in the relative strength of the 6.2 and 7.7 μm CC modes with respect to the 11.2 μm resonance.

Observationally, PAH band ratios have indeed been reported to vary, and early reports include the work by Bregman et al. (1989), who have charted the PAH emission across the Orion Bar in 6 equally spaced positions, 5" apart. They measured the intensity in the 3.3, 7.7, 8.6 and 11.3 μm bands, and variations in the ratios are clearly apparent. Quantum chemical calculations (e.g. DeFrees et al. 1993; Bakes et al. 2001) demonstrate that the ratio between 6.2, 7.7 and 8.6 μm emission on the one hand and 11.3 and 12.7 μm emission on the other depends on the ionization fraction of the PAHs, and a dependence of these band ratios on the impinging radiation field G_0 can be derived. Indeed, the 8.6/11.2 band ratio appears to trace the level of ionization well in reflection nebulae, with the highest ratio and therefore the highest degree of ionization closest to the star and decreasing with increasing distance (Joblin et al. 1996; Bregman & Temi 2005), although Uchida et al. (2000) report that they do not see this behaviour and attribute this to uncertainties in the feature extraction method. The 7.7/11.3 ratio is insensitive to changes in the radiation field at low and intermediate levels of irradiation $\lesssim 1000G_0$, as Chan et al. (2001) demonstrate with a study of ~ 800 diffuse Interstellar Medium sightlines. For more intense radiation fields, the (6.2, 7.7, 8.6)/11.2 ratio can effectively used as a probe for the radiation field, as demonstrated by Berné et al. (2009), who use the 6.2/11.3 ratio to obtain G_0 for the bright PDR Mon R2.

With the *Spitzer* Space telescope (hereafter *Spitzer*) it became possible to study four of the five most prominent PAH features in a much larger variety of environments, and to obtain more spatial information than before. Reflection nebulae, such as NGC 7023 have been subject to extensive research (Fleming et al. 2010; Boersma et al. 2013, 2014; Andrews et al. 2015; Boersma et al. 2015), showing a clear trend between 6.2 or 7.7 emission on the one hand and 11.3 emission on the other hand with the intensity of the radiation field, and the distance to the illumination star.

A gradient in the corresponding ratios can be observed across NGC 7023. The results for other reflection nebulae are similar (Fleming et al. 2010; Andrews et al. 2015; Boersma et al. 2016). Other ratios, such as 12.7/11.3 are more constant (Fleming et al. 2010). It is found that 7.7/11.2 is not a good probe of the degree of ionization, and that 8.6/11.2 and, surprisingly, 11.2/12.7 give better results when looking to determine the charge of the PAH molecules (Boersma et al. 2014, 2015).

Stock et al. (2013) targeted compact H_{II} region IRAS 12063–6259, and compared the spatial variation of the 6.2, 7.7 and 8.6 μm band strengths against the 11.2 μm feature. The ratios are found to vary by a factor of 2–3 across the region, while smaller variations ($\sim 30\%$) are observed in the 6.2/7.7 and the 12.7/11.2 ratios.

In a recent paper, Boersma et al. (2018) compared the 6.2/11.2 band ratio between a number of different types of regions: a reflection nebula (NGC 7023), an H_{II} region (M17) and a Planetary Nebula (PN; NGC 40). As mentioned before, a strong gradient (1.0–4.0) was observed towards the reflection nebula, while the H_{II} region showed a more structured appearance with the ratio ranging between 1.0 and 2.0. The ratio is mostly constant around 0.5 in the PN. In NGC 7023 a gradient in PAH size is also seen, with larger PAHs coinciding with higher ionization fractions. At the same time, the ionization fraction is anti-correlated with the H₂ column density.

Supernova (SN) remnants represent another class of objects exhibiting PAH emission, and Seok et al. (2012) analyse the (6.2, 7.7)/11.3 band ratios in N49. The values are most lower than in star forming regions and galactic diffuse emission, and point to mostly neutral PAHs. Their Figure 8 provides a useful overview of the relevant PAH ratios between different classes of objects, with the SNe at one extreme and PN, reflection nebulae and H_{II} regions at the other extreme. Galaxies are located at intermediate points, as their integrated spectra average over a multitude of environments. Galliano et al. (2008) further compared Galactic and extragalactic spectra by targeting three different environments: Galactic H_{II} regions, Magellanic H_{II} regions and galaxies. Spatial information is available for IC 342, M17, M51, M82, M83 and 30 Dor. In the galaxies M82 and M51 a broad range of values for the 6.2/11.3 ratio is observed, with the highest values found along the edge-on disk (for M82) and along the spiral arms in the nucleus (for M51).

A widely used diagnostic method was proposed by Draine & Li (2001), who compare the 11.3/7.7 and the 6.2/7.7 ratios to constrain the degree of ionization and the typical size of the PAHs simultaneously. This method has been widely applied in studies of extragalactic PAHs. The ratios are shown to vary between galaxies, as is for instance demonstrated by the nearby sample of SINGS galaxies (Smith et al. 2007b), starforming galaxies (O'Dowd et al. 2009), and starburst galaxies (Brandl et al. 2006). The authors of the latter study do not find any correlation between radiation field tracers, such as the [NeIII]/[NeII] ratio, and the 7.7/11.2 degree of ionization tracer, and attribute this to a resolution effect where spatial fluctuations on smaller scales in the 7.7/11.2 have been averaged out in the integrated spectra. Thus, it is important to investigate the spatial variation of the PAH band ratios within galaxies.

For instance, active galaxy M82 is shown to exhibit spatial variation in the degree of ionization and PAH size in particular in the wind (Förster Schreiber et al. 2003; Beirão et al. 2008, 2015), showing that a large fraction of the sightlines in the winds are dominated by large PAHs (> 250 C atoms), and that charges are closer to neutral than fully ionized. This seems to be at odds with the results by Yamagishi et al. (2012), who include the $3.3 \mu\text{m}$ feature observed with AKARI in the analysis, demonstrating the survival of small PAHs 2 kpc into the halo. Within galaxies however, Gordon et al. (2008a) show that for instance in M101 the ratio of $(6.2, 7.7 \text{ or } 8.6)/(11.3 \text{ or } 12.7)$ does not change much from one region to the next. A systematic study of 15 local LIRGS (Pereira-Santalla et al. 2010a) shows that the $11.3/6.2$ value is lowest in the nuclei of these galaxies, and it is argued that the ratio is sensitive to the star formation activity. In regions of star formation, the 7.7 band is strong, while the $11.3 \mu\text{m}$ band originates more from the diffuse emission. Haan et al. (2011) have looked for systematic trends in the $11.3/7.7$ ratio along the Toomre sequence, but find that variations of this band ratio within the galaxies exceed any systematic trend along the sequence.

It is clear that global ratios as observed in the integrated spectra of galaxies do not match the PAH band ratios observed in specific small scale environments. Even in the cases where spatial information is available for external galaxies, the resolution is such that the step from small scale environments, such as individual HII regions, reflection nebulae or PNe, to the size of a resolution element in a nearby active galaxy, such as M82, is so large that it averages out the information contained in the band ratios. The Large and Small Magellanic Clouds (LMC, SMC), however, at distances of 50 and 60 kpc, are close enough that this gap can be bridged, and the variation of PAH band ratios at intermediate scales can be studied. Only a small number of studies have done so far. Vermeij et al. (2002) has analysed integrated PAH spectra of HII regions in the LMC, SMC and Milky Way, and found that the PAH band ratios are segregated in a sequence between these three galaxies. However, preceding the *Spitzer* era, this study lacks spatial information. Second, as stated before, Galliano et al. (2008) include three Magellanic HII regions in their analysis, but spatial information is only available for 30 Dor. The third relevant study is the work by Sandstrom et al. (2012), who obtained *Spitzer*-IRS maps of six star forming regions in the SMC. They calculate PAH band ratios in each spatial resolution point and compare the results with the SINGS galaxy sample (Smith et al. 2007b). They find that in particular the $7.7 \mu\text{m}$ band is weak compared to the 6.2 and $11.3 \mu\text{m}$ features, and that the $8.6 \mu\text{m}$ band is weak compared to the integrated PAH emission. In general, the PAHs in the SMC are more neutral, and relatively small, compared to the SINGS average. Unfortunately, Sandstrom et al. (2012) do not present maps of the PAH band ratios, and the emission characteristics are not in any way correlated with the location on the sky.

In this work we want to extend on the work by Sandstrom et al. (2012) by doing a PAH band ratio analysis for regions in the LMC. In total, 23 regions have been mapped with *Spitzer*-IRS, and most of these observations have been taken in the context of the SAGE-Spec legacy program (Kemper et al. 2010). The data of twelve of these regions have been already analysed for H_2 emis-

sion (Naslim et al. 2015). In this work, we present XXX of the available 23 spectral maps (the remaining maps do not have sufficient signal-to-noise to be included in this analysis), and measure the PAH band ratios in each spatial point and analyse the overall trends. Spatial trends are included in this analysis.

This paper is organized as follows: XXX

2. Observations

The regions we analyse are a subset from the full SAGE-SPEC and S⁴MC dataset. The selection was made to cover a range of physical conditions. The critia used are the following. Signal to noise ratio: some maps have too weak emission throughout the region in order to reliably measure PAH band ratios. The predominance of highly ionised gas as traced by S IV and CO detections. The selected regions also exhibit a range of “topologies”, where some regions are clearly powered by an embedded young star clusters, while others are more externally excited. We have decided to exclude the 30 Dor dataset (PI Indebetouw) because large parts of the observations are affected by strong negative artifacts, probably due to bright sources in the peak-up window, which make it difficult to reliably measure the PAH bands. Moreover, because of the very strong hot dust continuum in the 30 Dor region, the PAHs bands are weak in band-to-continuum ratio adding to the difficulty to measure the individual band strengths.

The selected regions are listed in Tab. 1 and presented in Fig. 1 and 2. The area targeted with Spitzer/IRS (yellow) is shown on top of a false colour composite with ionised gas ($H\alpha$) in blue, stellar photospheres in green (IRAC 2 at $4.5\ \mu m$) and PAH dominated (IRAC 4 at $8.0\ \mu m$) in red. Eventhough the linear extend covered is large by IRS standards (1 to several arc-minutes; $\sim 20\text{--}80\ pc$), the resulting spectral cubes are still small compared to the physical regions and in some cases the stars that are exciting most of the emission are not even within the field-of-view (e.g. near LMC N148 and N55A). This means that we will have to take special care when discussing the spatial dependence of the observed emission.

3. Data reduction

The data reduction process is started using the basic calibrated data (BCDs) (Pipeline version 10, Calibration Set C18.18POST44.A) for the science and background observations (see Tab. 1) downloaded from the *Spitzer* heritage archive¹.

The spectral cubes have been produced using CUBISM (Smith et al. 2007a) in the following manner which involves a number of non-standard steps. The observing strategy that we chose optimises the area covered on the sky at the expense of reduced redundancy. The extra steps are necessary to mitigate the effect of limited redundancy on the quality of the final cubes. In essence, the extra steps are “tricks” to minimise the number of pixels that have to be flagged as rogue pixels.

¹ <http://sha.ipac.caltech.edu>

Table 1. Table of observations

AOR Name	Region	α^a [J2000]	δ^a [J2000]	AORkey	Background AORkeys
LMC					
lmc-diffreg01	near N148	5:32:02	-68:28:11	22460928	22462976, 22471680, 22472960, 22479616
lmc-diffreg05	near N120	5:55:54	-68:11:58	22461952	22464000, 22464256, 22464512
lmc-diffreg10	near N55A	5:32:23	-66:28:40	22479872	22472192, 22472448, 22473216, 22480128
lmc-hii01	N4	4:52:07	-66:55:29	22469120	22462976, 22471680, 22472960, 22479616
lmc-hii03 ^b	N11B	4:56:50	-66:24:51	22469632	22464000, 22464256, 22464512, 22472192, 22472448, 22473216
lmc-hii06 ^b	N105	5:09:55	-68:54:06	22470400	22462976, 22471680, 22472960, 22479616
SMC					
irsm-smcn22sh2	N22 north	0:48:04	-73:13:59	18262016	18265856, 18266368
irsm-smcn22sh1	N22 south	0:47:57	-73:17:37	18261760	18265856, 18266368
irsm-smcn66sh2	N66 north	0:59:15	-72:09:06	18262784	18265856, 18266368
irsm-smcn66sh1	N66 south	0:58:57	-72:12:29	18262528	18265856, 18266368
irsm-smcbarsh1	SW bar 1	0:48:21	-73:05:44	18265088	18267904, 18268160, 18268928
irsm-smcbarsh3	SW bar 3	0:45:35	-73:22:51	18265344	18267904, 18268160, 18268928

^a These coordinates correspond to the approximate centers of the spectral cubes after combining the short-low orders. ^b The following frames have been removed from the stack because of large artefacts: SPITZER_S0_22469632_0230_0000_5_bcd.fits, SPITZER_S0_22470400_0122_0000_4_bcd.fits, SPITZER_S0_22470400_0590_0000_4_bcd.fits.

We create a first background image using the mean of the sigma-clipped background observations listed in Table 1 which includes more frames than is usual. This results in a less noisy image but with an increased number of rogue pixels that do not match the mean level of this pixel during the science observation. Next, we create a stacked image of the entire science observation with this background removed. This stacked image is analysed to identify isolated deviant pixels, i.e. pixels that *systematically* deviate from their neighbours. These are defined as single pixels with a difference larger than a given threshold (100%) from the 3 pixel median both in the x (wavelength) and in the y (spatial) direction. We impose that the pixel needs to be deviant in both directions to avoid spuriously flagging pixels as a result of sharp spectral features (emission lines) or sharp spatial features (bright compact sources). We determine the difference between the value of flagged pixels and the median of their neighbours and add this to the background image. In this way these pixels no longer appear as outliers when subtracting this background from the stacked image. Note that, this procedure is only correcting for any average offsets between the zero-level of the pixel during the science observation and the background observations. It is unable to correct truly rogue pixels, i.e. pixels that behave erratically during the science observation.

Using the thus constructed background, we apply an automatic sigma-clipping to remove the systematic outliers (Cubism option: Auto-Gen Global Bad Pixels – Sigma-Trim = 5). All other rogue pixels are flagged manually through visual inspection of the individual frames and the resulting spectral cube in which rogue pixels appear as offset stripes in the scanning direction, i.e. the direction in which consecutive spectra have been taken.

All pixels are rogue pixels to a certain extent and depending on the contrast-level one selects for visual inspection, many pixels that cause striping in the extended emission, i.e. the lowest brightness levels, can be identified. This is particularly true for our datasets because of the limited redundancy. We only flag the most outstanding rogue pixels and keep the pixels which cause

low-level striping. This low-level striping is removed in a dedicate post-processing step. This step consists of determining for each column, i.e. the scanning direction, of each wavelength plane of the spectral cube the mean value of the lowest quartile, i.e. the mean extended emission level. The difference between this mean background in the cross scanning direction and a 5-point box-smoothed mean background is subtracted from the wavelength plane to remove column-to-column baseline variations.

3.1. Beam matching

The outcome of the processing from cubism is cleaned individual spectral cubes for each spectral order. The different orders do not share the same pixel scheme and the beamsize varies as a function of wavelength. In order to obtain one spectral cube per object where each sky pixel contains an independent, full spectrum we apply the following method, which is inspired by the method outlined in Gordon et al. (2008b). A key difference between our treatment and the treatment in Gordon et al. (2008b) is that we use Gaussian point-spread-functions (PSFs) based on measured beam sizes instead of PFSs using the STINTIM software.

We create a kernel for each wavelength plane to convolve to a common spatial resolution. The target beam is chosen to be a 2D Gaussian beam with a full-width-at-half-max (FWHM) of 3.8 arcsec, appropriate for a wavelength slightly larger than the (PSF) of the longest wavelength point ($14 \mu\text{m}$). The size of the input PSFs for each wavelength is based on the measurements of (Pereira-Santalla et al. 2010b). These authors measured the FWHM in the direction of the slit (parallel; \parallel) and in the perpendicular (\perp) direction of a 2D Gaussian profile fit to point sources in the spectral cubes produced by CUBISM (their Fig. 25). The FWHM measurements show some fluctuations as a function of wavelength which we prefer not to include in our synthetic PSFs. The global behaviour of the measured FWHMs is well captured by the following simple approximations:

$$\begin{aligned} \forall \lambda < 13.25\mu\text{m} : \text{FWHM}_{\parallel} [\text{arcsec}] &= 2.8 + 0.035 \times \lambda [\mu\text{m}] \\ \forall \lambda < 15.5\mu\text{m} : \text{FWHM}_{\perp} [\text{arcsec}] &= 3.8, \end{aligned} \quad (1)$$

where λ is the wavelength. At longer wavelengths we assume that the FWHM in both directions corresponds to the diffraction limit of the telescope ($\text{FWHM} [\text{arcsec}] = 0.25 \times \lambda [\mu\text{m}]$). The convolution kernel to blur (convolve) the image at a given wavelength to the target beam is obtained by ratioing the fourrier transform of the target PSF by the fourrier transform of the PSF at that wavelength. An advantage of using Gaussian PSFs is that the thus obtained kernel does not exhibit high frequency noise, i.e. strong small scale fluctuations in the convolution kernel. Therefore, the low-pass filtering procedure that is applied in Gordon et al. (2008b) is not required in our method.

We define a common spatial reference grid which encompasses the field-of-view of all orders and subsequently reproject the wavelength planes of each order onto this common grid using SWARP from AstroMatic². We retain the data of the orders in the following wavelength ranges: SL2 be-

² <http://www.astromatic.net>

tween 5.23 and 7.49 μm , SL3 between 7.4 and 8.5 μm and SL1 between 7.53 and 14.02 μm . We obtain the final spectrum at each sky-position by rebinning on a regular wavelength grid, those part of the spectrum where the orders overlap, i.e. 7.4–7.49 μm and 7.53–8.5 μm . Any sky-positions in the resulting cube which are not observed by all spectral orders of interested are masked and not considered in our analysis.

4. Spectral Fitting Method

Each independent spectrum (pixel by pixel) is decomposed using our spectral fitting code. The spectra are separated in atomic line, stellar continuum, dust grain and individual PAH emission feature contributions. The details of the fitting procedure are given in Appendix 8. An important step in the decomposition is the uncertainty estimates on the derived parameters. These are obtained using a Monte-Carlo (MC) approach in which we add a noise spectrum to the original spectrum. The wavelength dependent amplitude of the noise spectrum is dictated by the noise properties of the original spectra. In essence we generate a “new realisation” of the input data that is consistent with original data and their uncertainties. The perturbed spectrum is decomposed with the exact same routine and this is repeated many times. The distribution of the derived parameters (e.g. a line flux) is used to calculate its uncertainty.

Note that it is essential for some interesting ratios to measure the distribution of the ratios in order to get reliable uncertainties, instead of relying on the uncertainties of the nominator and denominator. This becomes necessary when the two measures are not independent. A good example of this is the surface brightness of the 8.6 μm feature over the surface brightness in the 7.7 μm complex. Because of blending, emission not attributed to the 8.6 feature will generally be attributed to the 7.7 complex.

5. Results

PAH Maps PAH/CONT Maps

Main ratio

Other bands

We present the maps of the integrated PAH intensity based on the spectral decomposition in Fig. 3 and 4. Because a large part of the PAH intensity is emitted in the 7.7 μm complex, that is picked up in the IRAC4 filter the maps resemble the red channel in the overview figures (Fig. 1 and 2).

One of the most striking aspects that these maps show is the general difference between the regions studied in the LMC and the SMC. The surface brightness of the LMC regions is generally higher than in the SMC and much more extended (Fig. 3 and 4). Specifically, the largest structures, i.e. connected emission regions in the LMC maps, with a surface-brightness per pixel above $2 \cdot 10^{-6} \text{ W m}^{-2} \text{ sr}^{-2}$ (red and orange colours in the PAH maps) extent over sizes up to $\sim 20 \text{ pc}$ in the LMC,

while in the SMC only tiny isolated pockets of emission reach such strong PAH emission. This is also clearly seen in the PAH strength scatter diagram (Fig. 7).

The maps of the PAH-over-continuum ratio, shown in figures 5 and 6, exhibit very strong variations. Most of the individual maps span a range larger than a factor of 30. The most notable exceptions are N148 and N55A that show a more moderate range of values because the very low values are missing. These regions are also the faintest regions in terms of surface brightness among the LMC regions. The low values of the PAH-to-continuum ratio coincide with the regions dominated by ionised gas as traced by S IV and these two specific maps exhibit little ionised gas.

The regions in the SMC exhibit much higher PAH-to-continuum values at low surface brightness. Note that the SMC maps are also larger in parsec than the LMC maps. As a result, the lines-of-sight that sample the more remote regions, that exhibit faint mid-IR continuum emission are therefore more numerous in the SMC maps.

An executive summary of the main results is temporarily given here. They are discussed in more detail below.

- There are significant variations in PAH surface brightness, PAH to continuum ratio and in PAH band ratios.
- These variations occur within the various regions but the most systematic differences are observed between regions and between the LMC and the SMC.
- the 6.2/11.2 and 7.7/11.2 correlate with a slope of ~ 1 which means that ionisation is the main driver of the variation.
- The LMC regions exhibit more high 7.7/11.2 than does the SMC
- The spatial trends in the variations are much less evident.
- There is a dependence of the observed PAH band ratio (7.7/11.2) on the PAH surface brightness. The lowest ratios correspond to low surface brightness.
- The SMC having globally lower surface brightness also globally exhibit a lower 7.7/11.2 ratio.
- Because the low ionised l.o.s. are faint and because they are often close to brighter and more ionised regions the “typical” (median) measured ionisation increases with beam-size.
- We find for the first time a correlation (slope ~ 0.2) between the continuum slope (mid-IR to $100 \mu\text{m}$) and the ionisation albeit with a large scatter.

5.1. Differences between SMC and LMC

Among our observations we detect significant differences between the PAH emission maps of the LMC and SMC regions, respectively. The regions that are bright in the LMC (red and orange colors in Fig. 3 and 4) are more extended in the LMC than in the SMC. The largest structures in the LMC (N105) are $> 80''$.

5.2. Region to region variations

One of the main drivers behind the observed range of band ratio variations is systematic differences between regions even within the same galaxy. In most of the scatter plots that we have inspected values from one region tend to clutter together but may be significantly offset from other regions. We show the most striking example of this is Fig. ??.

5.3. Main Feature Maps

We show in Fig. 3 and 4 the PAH surface brightness maps. The PAH surface brightness is obtained by integrating over all the PAH emission features after the spectral decomposition. The PAHs maps closely resemble the IRAC4 emission (red) in Fig. 1 and 2, which measures predominantly the strong $7.7\ \mu\text{m}$ complex of the PAHs. We also show in contours the surface brightness of the [S IV] line as an indication of the l.o.s. towards the highly ionised gas. In almost all regions, with the notable exception of SMC N22 North, the brightest PAH emission is found close to, but offset from, the brightest [S IV] emission. Conversely many lines-of-sight with strong [S IV] are relatively faint in PAHs. This “anti-correlation” qualitatively matches the view that the ionised gas should be devoid of PAHs due to photo-dissociation while the brightest PAH emission originate from the PDRs surrounding the ionised bubbles.

There is a striking distinction between the LMC and the SMC regions in terms of PAH surface brightness. The highest surface brightness (orange color) is ubiquitous in the LMC and only found towards a small number of bright knots in the SMC. Conversely, large parts of the SMC regions exhibit lower surface brightness than observed in most of the LMC targets (light blue color). As a result of this any trends we find depending on brightness will be dominated by the SMC targets at the low end and by the LMC regions at the bright end.

5.4. Main Ratios Maps

Here we discuss the spatial behaviour of the several diagnostic line and PAH band ratios. Given the diversity of the regions and the large number of beams to consider, we first discuss the behaviour of the ratios within the individual maps. The ratio maps we show (Figs. ??– ?? are designed to transmit at the same time the spatial variations and the significance of the individual measurements.

To this end the plots are designed in the following manner. The colors of the points in the maps show the value of the ratio of interest. The size of the points inside the maps is dependent on the significance of the reported ratio. When the ratio becomes less reliable (see below), we reduce the size of the point. Beyond this the size of the point decrease with decreasing reliability of the measurement. This way of representing the data prevents the dynamics range to be dominated by regions with little signal where the measured ratios will vary enormously due to the large uncertainties without having to resort to applying arbitrary cuts. Moreover, we choose the ratio such that for most of the beams the nominator is larger than the denominator.

The reliability criterion of the ratio (X/Y) is based on their sum ($X+Y$). Locations where the ratio is aberrant because both X and Y are small compared to the noise are not interesting. On the contrary, places where the ratio is driven by one of the measures being weak and the other being strong, are very interesting.

We have kept the dynamic range of the color-scale identical for the different regions, if the data permit it. This facilitates region-to-region comparisons. We further show in contours the summed emission of all the PAH bands.

The highest dynamical range in PAH ratio (more than two orders of magnitude) is found in the PAH to IRS-continuum. We show the corresponding maps in Fig. 5 and 6. Very low values are systematically found towards ionised gas dominated l.o.s, i.e. bright S ivemission. This is the combined result of photo-destruction of the PAHs (e.g. ?) and the boosting of the hot-dust continuum in the ionised gas (e.g. ?). Interestingly the brightest PAH emission is coming from low PAH/continuum regions while the highest PAH/continuum is alway coming from the faint diffuse sight-lines (see also Fig. 7). Eventhough the global trend is for the ratio to increase towards fainter areas, there are also some PAH-faint regions that exhibit, low ratios, most notably around the edges of the ionised bubble of SMC-N66. Possibly these correspond to low density channels where ionising radiation is escaping.

5.5. 11.25 versus Complex 7.7

We show the ratio of the $7.7\text{ }\mu\text{m}$ complex attributed predominantly to CC stretching modes over the $11.25\text{ }\mu\text{m}$ CH out of plane bending mode bands (Fig. 9 and 9). Laboratory measurement indicate that the relative strength of these two is sensitive to the charge of the PAH molecules (Hudgins et al.) Perusal of the ratio maps shows that:

- There are significant variations in the observed ratio ranging between 2 and 10.
- There are quite significant differences between regions. In particular many regions in the LMC exhibit ratios around 4–6 (purplish) while most of the SMC regions have values between 2–4 (blueish).
- Within several regions (N120, N4, SWBar1b) the brightest PAH emitting regions exhibit higher than typical values, which means that spatially averaged spectra will be biased to yield higher ratios. This bias is more clearly demonstrated in Fig. 11 where the median value increases from 2 to 6 from 4e-7 to 2e-5 XXX units in PAH surface brightness.
- Besides the very brightest (central) regions exhibiting high ionisation, there is strikingly little coherent structure in the maps. Eventhough each map exhibits factor of a few variations in this band-ratio, one cannot discern a clear radial dependence of the ionisation on the projected distance to the exciting stars. A very good example of this is N11B where most of the exciting stars are located to the south of the molecular complex, but the entire complex shows similar ratios.

6. Summary and discussion

Focussing on the most important band ratio in terms of luminosity and diagnostic power (7.7/11.25) our results can be summarised as follows. We find a significant variation of band ratios between 2 and 10. The observed ratio is very tightly correlated with the 6.25/11.25 band ratio for most of the studied lines of sight (Fig. 13). We interpret this as evidence that the main driver for the observed PAHs emission spectra variations is the average charge state of the PAH molecules, because the main effect of charge on the PAHs is to change the relative strength of the CC-modes relative to the CH-modes (6.25 and 7.7 vs 11.25) without a systematic effect on the relative strength of the individual CC modes (6.25 vs 7.7) (refXXX).

In this view, the l.o.s. with highest observed 7.7/11.25 ratios (~ 10) correspond to the ISM with the most ionised PAH population. Because the charge state is determined by the ionisation rate over recombination rates (G_0/n_e) this could correspond to either close to strong young stars, i.e. high radiation field, or lower than typical densities i.e. little recombination. However, the spatially resolved band ratio maps (Fig. 9 and 10) are not easily so interpreted in this framework. A significant part of the dynamic range in band ratios is not due to variations within the map (distance to the exciting stars nor density variations) but systematic offsets between the different regions.

Careful inspection of the various maps shows that within most regions the locations closest to the dominant exciting stars – those regions that are also brightest in their total PAH emission – exhibit a bit higher PAH ionisation degree than the immediate surroundings. The best examples of this behaviour are observed in N4 and N120 in the LMC (Fig. 9). The fact that these two regions are showing this behaviour most clearly is probably related that within those maps the ISM irradiation is dominated by a central embedded source (Fig. 1).

We are unable to discern significant spatial/radial trends, beyond the immediate vicinity (within a few parsec in projection) of these “hotspots” even though there clearly are significant variations of the band-ratio throughout all regions. N11 and N105 in the LMC and SW Bar 3 in the SMC are very good illustrations of this. We interpret this lack of spatially coherent systematic behaviour as indications that 1) on the size scales of these maps ($\sim 50\text{--}100$ pc) the photons that excite the PAH emission can traverse relatively unimpeded and 2) that the overdense regions where these photons are absorbed to give rise to PAH emission exhibit a range of densities. Both these aspects, that are needed to understand the fluctuations of PAH ionisation degree throughout these regions, imply a very porous and clumpy ISM.

One interesting aspect that emerges from our analysis is that strong PAH surface brightness is selective in the PAH ionisation state.

6.1. 6.2 versus complex 7.7

We show the ratio of the $6.2\ \mu\text{m}$ band and the $7.7\ \mu\text{m}$ complex. Variations in this value could trace shifts in the typical size of the PAHs. In this interpretation higher ratios correspond to larger internal energy per mode i.e smaller molecules. Perusal of the ratio maps shows that:

- Most of the spectra show *very* similar ratios in a narrow range around 0.3.
- This is even more true when concentrating on those regions where the PAH emission is strong.
- Slightly lower values (larger PAHs?) are found in those regions neighbouring the harder radiation field/lower densities
- There is little systematic difference between the various regions with the exception of to 30Dor region.

6.2. Radiation field

We show a “poor mans” proxy for the hardness of the radiation field $\text{S}\,\text{IV}/\text{Ne}\,\text{II}$ in Fig. ???. This is only a proxy as it does not take into account the abundance of Ne and Si. We use this combination of lines because they are the best pair of lines available in the spectra we analyse.

These maps are mostly to show where the high ionised gas is. This quantity is probably more interesting as one of the axes in the scatter plots of band strength and ratio versus various physical condition tracers. As can be observed in most maps, the strongest PAH emission is most often near but not on the hot spots of hard radiation, as is expected if the dense PDRs are located near the sites of high-mass star formation.

6.3. Something ionised versus something neutral

The maps which show Ne II over PAH are probably not so interesting. These maps were prompted by the wish to see the mixing of ionised and neutral gas across the regions. However I think they mostly emphasise the variations of column density.

The next set of figure are radiation hardness (left) and ionised tracer over neutral tracer (middle) and the PAH 11.2/7.7 μm (right) to examine if the variations in this PAH ratio appear to be more driven by the radiation field or the density. At face value there are several series of maps where the middle panel and the right panel bear more resemblance. However for 30 Dor this does not appear to be the case.

6.4. PAH equivalent with (PAH/Continuum)

The dynamical range in the PAH to continuum ratio (PAH equivalent width) is largest in all the presented ratio. This is probably driven by a contribution of hot dust from ionised gas where the PAH emission is weakest. This is quite well visible in the maps where the parts of the maps on the side of the most intense radiation field have very low values.

7. Region by region analysis

In the following section some key maps of various ratios are repeated by now shown side by side to help in the comparison. In the final paper we will keep only one way of organising these figures of course.

Table 2. XXX

Region	α [J2000]	δ [J2000]	Remark
LMC N11B	4:56:51.127	-66:23:49.35	(halpha, 24um and brightest irac1 source star #3160 of parker92, KI, spectrum is sum of ste
LMC N120	5:09:50.675	-68:53:05.46	Probably deeply embedded hot star. Not matched in Bonanos. Spectrum could be silicate ab
SMC N22	0:48:08.519	-73:14:54.88	LHA 115-N 26 – Planetary Nebula? – Testor 2014 talks about this as a compact Hii region
SMC N22	0:47:52.399	-73:17:11.34	Strong 10 silicate absorption this should reduce the 77/11 ratio. #19 in Testor14
SMC N66	0:59:05.461	-72:10:35.77	central cluster of NGC346 Very strong continuum source with a weird emission bump. Not
SMC N66	0:59:09.253	-72:10:57.63	Embedded source strong silicate absorption. In this case it boosts the 77/11 ratio (contrary to
SMC N66	0:59:05.926	-72:11:28.71	appear like a stellar continuum in addition to the ISM spectrum. There really is a very bright

^a SWS observing mode used (see de Graauw et al. 1996). Numbers in brackets correspond to the scanning speed.

7.1. near N148

7.2. near N120

7.3. near N55A

7.4. N105

7.5. N4

7.6. N11B

7.7. 30 Doradus

7.8. Scatter plots and trends

7.9. Specific regions and relation to the exciting stars

Inspection of the resulting spectra and the line ratios shows that some of the brightest lines of sight exhibit very peculiar mid-IR spectra with a very wide range of properties. Our interpretation is that this is because these regions represent a “mixed-bag” of source types. In particular, there are some very bright, embedded sources among them. These sources are typified by very strong mid-IR continuum emission. A list of the most obvious such sources is given in Tab. 2 and their corresponding spectra are shown in Fig. 15. Note that this list is evidently incomplete and only gives the coordinates where the emission due to the embedded stars dominates the emission. Also note that this “classification” is by construction dependent on the spatial resolution that we used. The main conclusion from inspection is that all these lines of sight indeed exhibit very strong continuum emission. Several sources show signs of 10 μm silicate absorption (2,4,6) which directly affects the measured PAH feature strengths. We exclude these singular lines-of-sight from the trend analysis.

8. Discussion

The zero-order conclusion of this work is that the PAH ratios across the LMC vary little. This statement still has to be quantified with a dispersion measure which takes the significant uncertainties on the measured ratios into account. We certainly do not observe a strong radial dependence of

the band ratios with distance to the exciting stars. The main variations are driven by 1) spatially coherent “pockets” of ISM which exhibit different ratios and 2) region to region offsets.

Due to the above the current scatter plots (not shown) are of only marginal interest. Most us the plots are dominated but the large number of points simply scatterd about the typical values and the “interesting” regions are hidden. Thoughts about how to approach this are very welcome.

I want to add to the current work the following aspects: Region-averaged ratios and spectra, these may include the pockets observed in the current maps but also the larger areas of very faint emission.

It might be interesting to try a cluster finding algorithm to identify such pockets that exhbbit particular ratios. I would be very happy to hear about other analyses that people might be interest in.

Acknowledgements.

References

- Andrews, H., Boersma, C., Werner, M. W., et al. 2015, ApJ, 807, 99
 Bakes, E. L. O., Tielens, A. G. G. M., & Bauschlicher, Jr., C. W. 2001, ApJ, 556, 501
 Begemann, B., Dorschner, J., Henning, T., et al. 1997, ApJ, 476, 199
 Beirão, P., Armus, L., Lehnert, M. D., et al. 2015, MNRAS, 451, 2640
 Beirão, P., Brandl, B. R., Appleton, P. N., et al. 2008, ApJ, 676, 304
 Bernard Salas, J., Pottasch, S. R., Beintema, D. A., & Wesselius, P. R. 2001, A&A, 367, 949
 Berné, O., Fuente, A., Goicoechea, J. R., et al. 2009, ApJ, 706, L160
 Boersma, C., Bregman, J., & Allamandola, L. J. 2014, ApJ, 795, 110
 Boersma, C., Bregman, J., & Allamandola, L. J. 2015, ApJ, 806, 121
 Boersma, C., Bregman, J., & Allamandola, L. J. 2016, ApJ, 832, 51
 Boersma, C., Bregman, J., & Allamandola, L. J. 2018, ApJ, 858, 67
 Boersma, C., Bregman, J. D., & Allamandola, L. J. 2013, ApJ, 769, 117
 Brandl, B. R., Bernard-Salas, J., Spoon, H. W. W., et al. 2006, ApJ, 653, 1129
 Bregman, J. & Temi, P. 2005, ApJ, 621, 831
 Bregman, J. D., Allamandola, L. J., Witteborn, F. C., Tielens, A. G. G. M., & Geballe, T. R. 1989, ApJ, 344, 791
 Chan, K.-W., Roellig, T. L., Onaka, T., et al. 2001, ApJ, 546, 273
 de Graauw, T., Haser, L. N., Beintema, D. A., et al. 1996, A&A, 315, L49
 DeFrees, D. J., Miller, M. D., Talbi, D., Pauzat, F., & Ellinger, Y. 1993, ApJ, 408, 530
 Draine, B. T. & Li, A. 2001, ApJ, 551, 807
 Fioc, M. & Rocca-Volmerange, B. 1997, A&A, 326, 950
 Fleming, B., France, K., Lupu, R. E., & McCandliss, S. R. 2010, ApJ, 725, 159
 Förster Schreiber, N. M., Sauvage, M., Charmandaris, V., et al. 2003, A&A, 399, 833
 Galliano, F., Madden, S. C., Tielens, A. G. G. M., Peeters, E., & Jones, A. P. 2008, ApJ, 679, 310
 Gordon, K. D., Engelbracht, C. W., Rieke, G. H., et al. 2008a, ApJ, 682, 336
 Gordon, K. D., Engelbracht, C. W., Rieke, G. H., et al. 2008b, ApJ, 682, 336
 Haan, S., Armus, L., Laine, S., et al. 2011, ApJS, 197, 27
 Hony, S., Van Kerckhoven, C., Peeters, E., et al. 2001, A&A, 370, 1030
 Jäger, C., Dorschner, J., Mutschke, H., Posch, T., & Henning, T. 2003, A&A, 408, 193
 Joblin, C., Tielens, A. G. G. M., Geballe, T. R., & Wooden, D. H. 1996, ApJ, 460, L111
 Kemper, F., Woods, P. M., Antoniou, V., et al. 2010, PASP, 122, 683

- Koike, C., Kaito, C., Yamamoto, T., et al. 1995, *Icarus*, 114, 203
- Laor, A. & Draine, B. T. 1993, *ApJ*, 402, 441
- Naslim, N., Kemper, F., Madden, S. C., et al. 2015, *MNRAS*, 446, 2490
- O'Dowd, M. J., Schiminovich, D., Johnson, B. D., et al. 2009, *ApJ*, 705, 885
- Peeters, E., Hony, S., Van Kerckhoven, C., et al. 2002, *A&A*, 390, 1089
- Pereira-Santaella, M., Alonso-Herrero, A., Rieke, G. H., et al. 2010a, *ApJS*, 188, 447
- Pereira-Santaella, M., Alonso-Herrero, A., Rieke, G. H., et al. 2010b, *ApJS*, 188, 447
- Rouleau, F. & Martin, P. G. 1991, *ApJ*, 377, 526
- Sandstrom, K. M., Bolatto, A. D., Bot, C., et al. 2012, *ApJ*, 744, 20
- Seok, J. Y., Koo, B.-C., & Onaka, T. 2012, *ApJ*, 744, 160
- Smith, J. D. T., Armus, L., Dale, D. A., et al. 2007a, *PASP*, 119, 1133
- Smith, J. D. T., Draine, B. T., Dale, D. A., et al. 2007b, *ApJ*, 656, 770
- Stock, D. J., Peeters, E., Tielens, A. G. G. M., Otaguro, J. N., & Bik, A. 2013, *ApJ*, 771, 72
- Tielens, A. G. G. M. 2008, *ARA&A*, 46, 289
- Uchida, K. I., Sellgren, K., Werner, M. W., & Houdashelt, M. L. 2000, *ApJ*, 530, 817
- Vermeij, R., Peeters, E., Tielens, A. G. G. M., & van der Hulst, J. M. 2002, *A&A*, 382, 1042
- Weingartner, J. C. & Draine, B. T. 2001, *ApJ*, 548, 296
- White, D. W., Gerakines, P. A., Cook, A. M., & Whittet, D. C. B. 2009, *ApJS*, 180, 182
- Yamagishi, M., Kaneda, H., Ishihara, D., et al. 2012, *A&A*, 541, A10

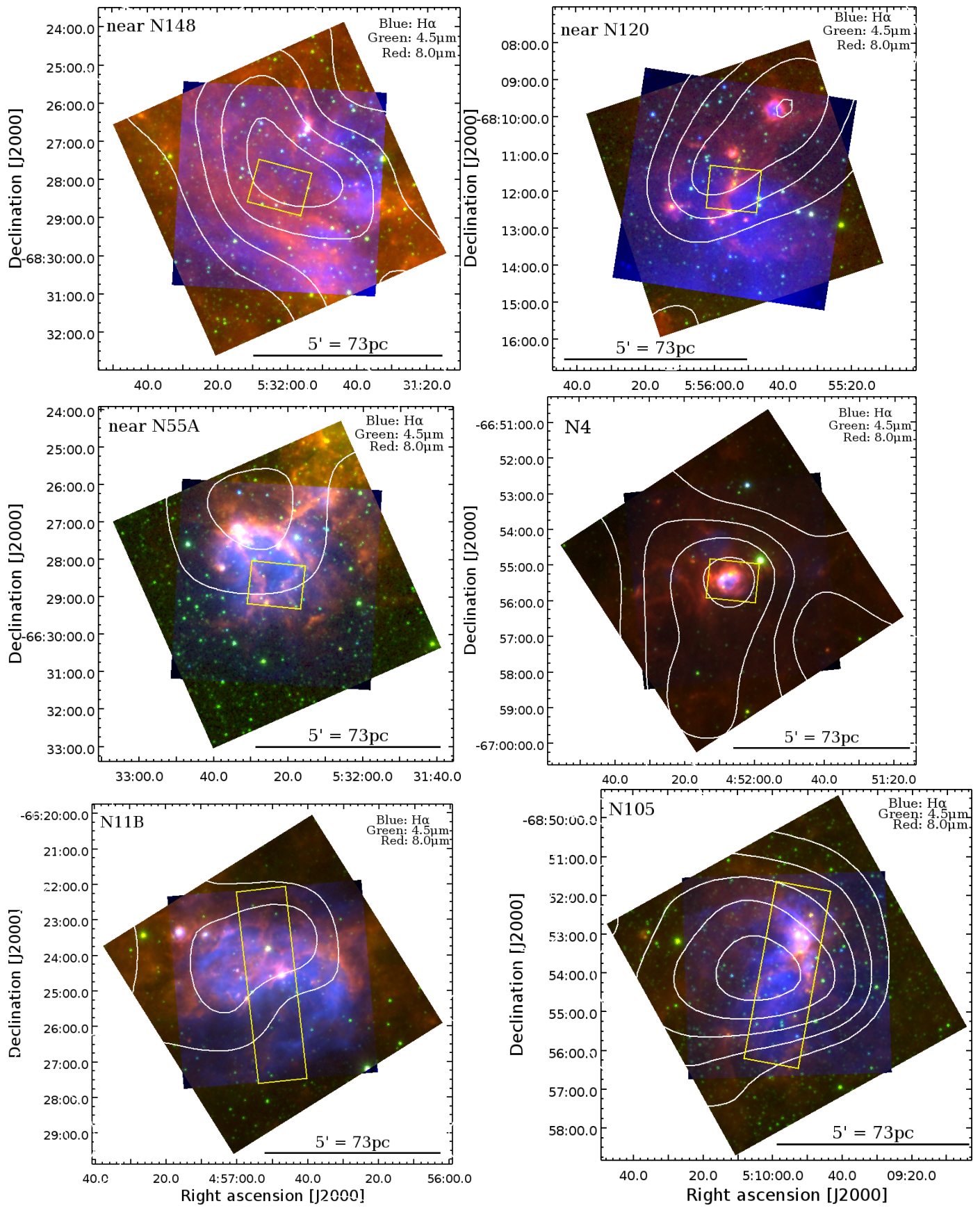


Fig. 1. XXX

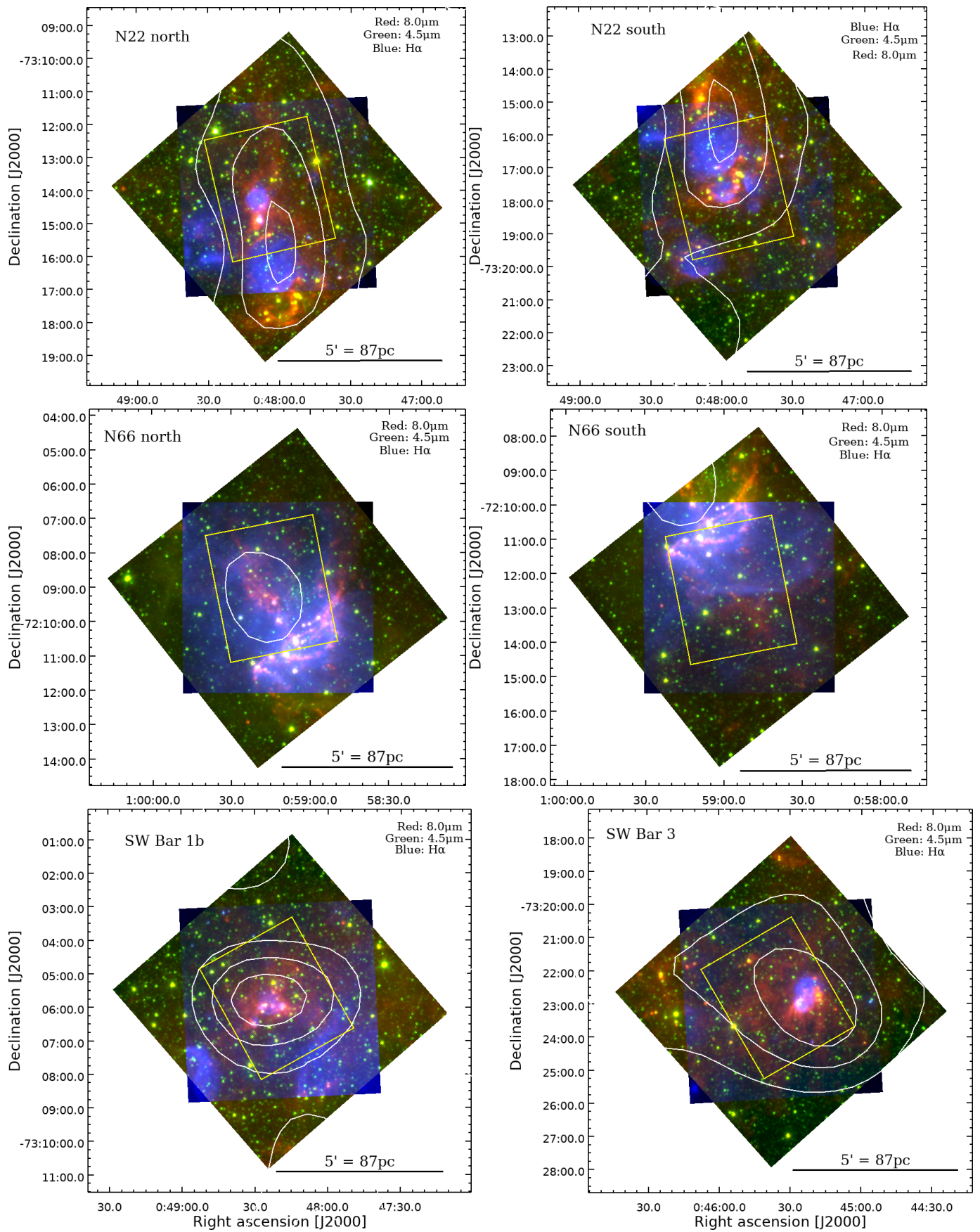


Fig. 2. XXX

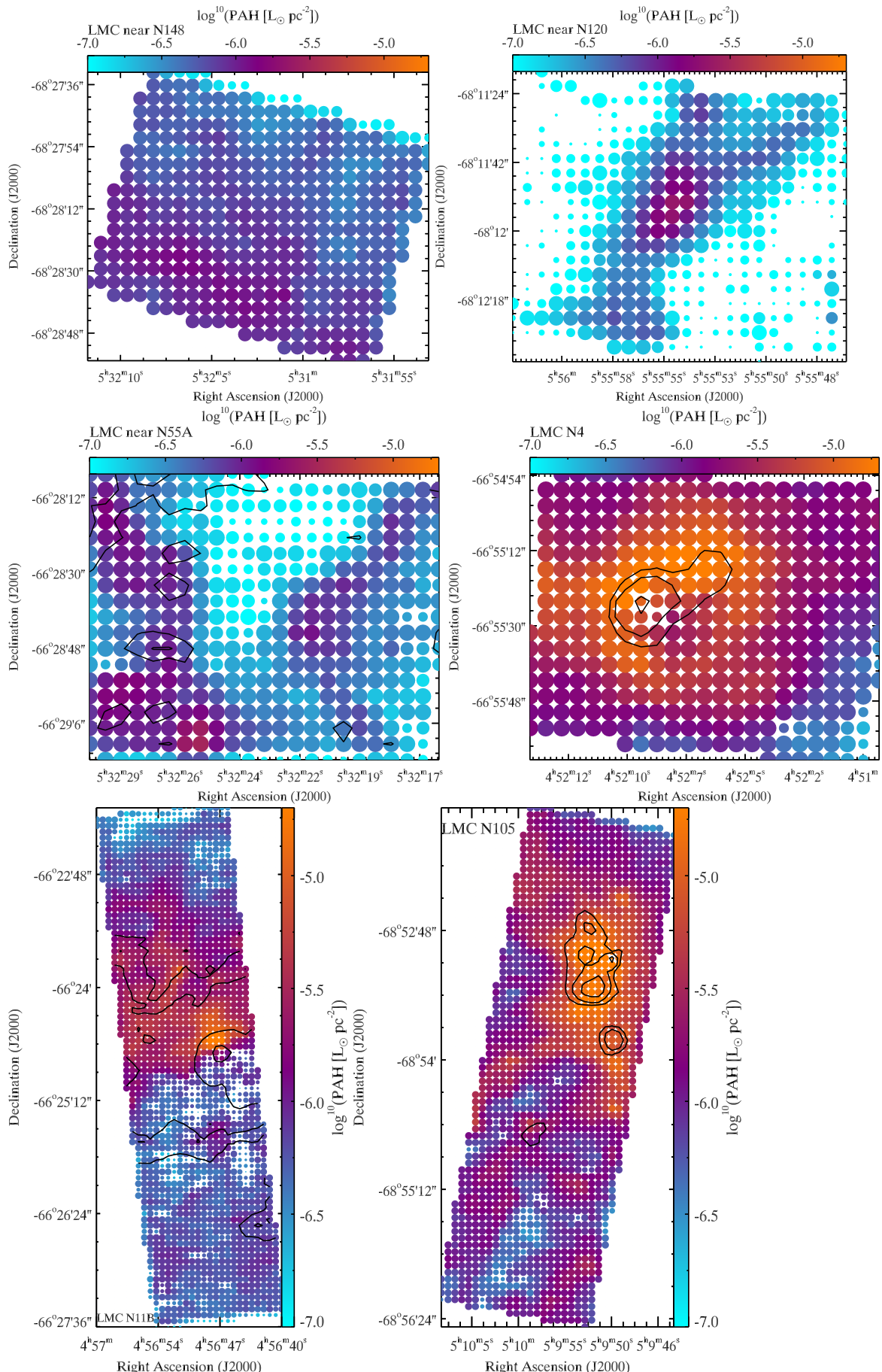


Fig. 3. PAH to continuum maps of the regions in the LMC. The size of each symbol is a function of the signal to noise (SNR), where the radius of the circle is proportional to SNR for SNR values below 8 and maximal above SNR equal 8.

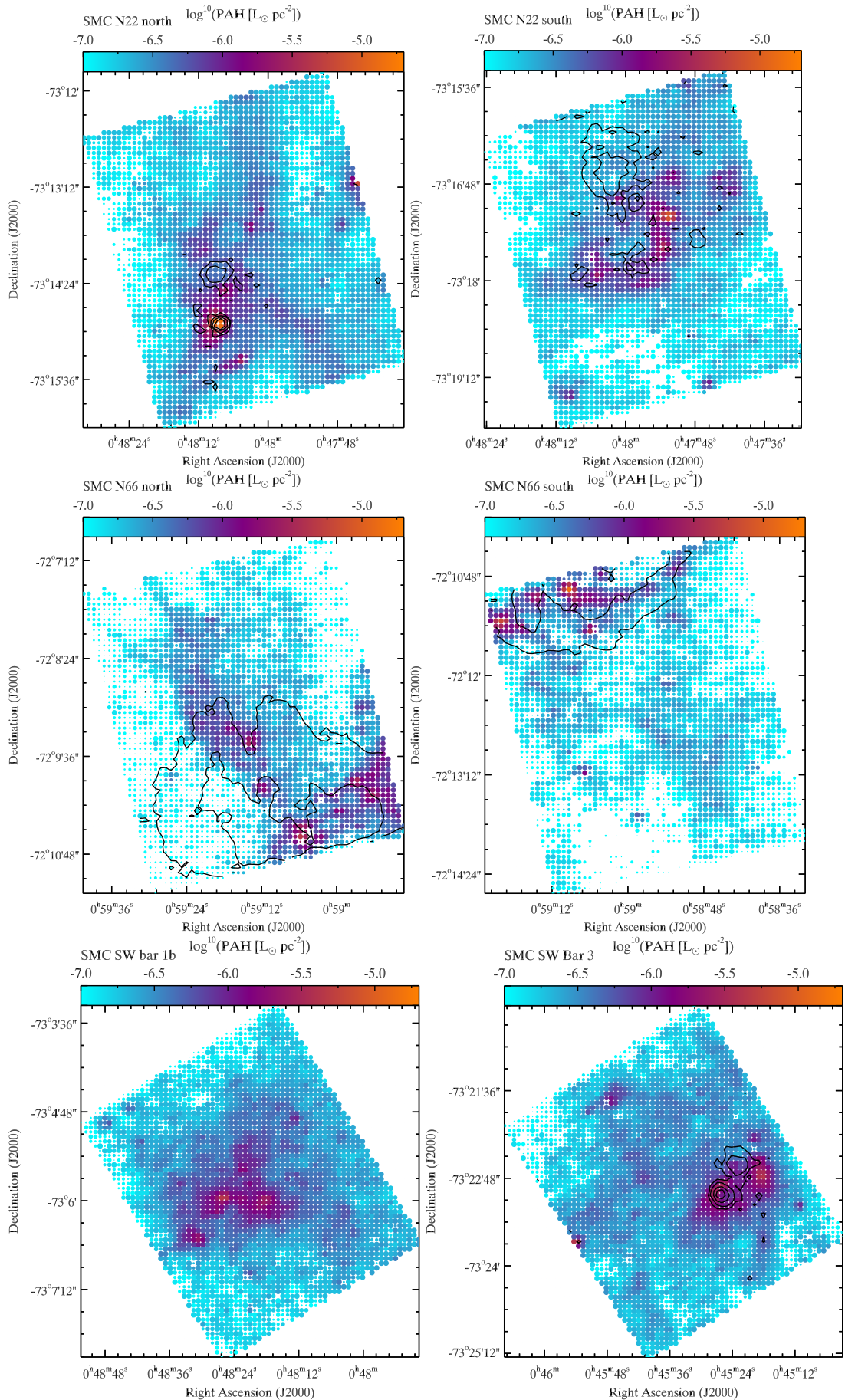


Fig. 4. PAH continuum maps of the regions in the SMC. The size of each symbol is a function of the signal to noise (SNR), where the radius of the circle is proportional to SNR for SNR values below 8 and maximal above SNR equal 8.

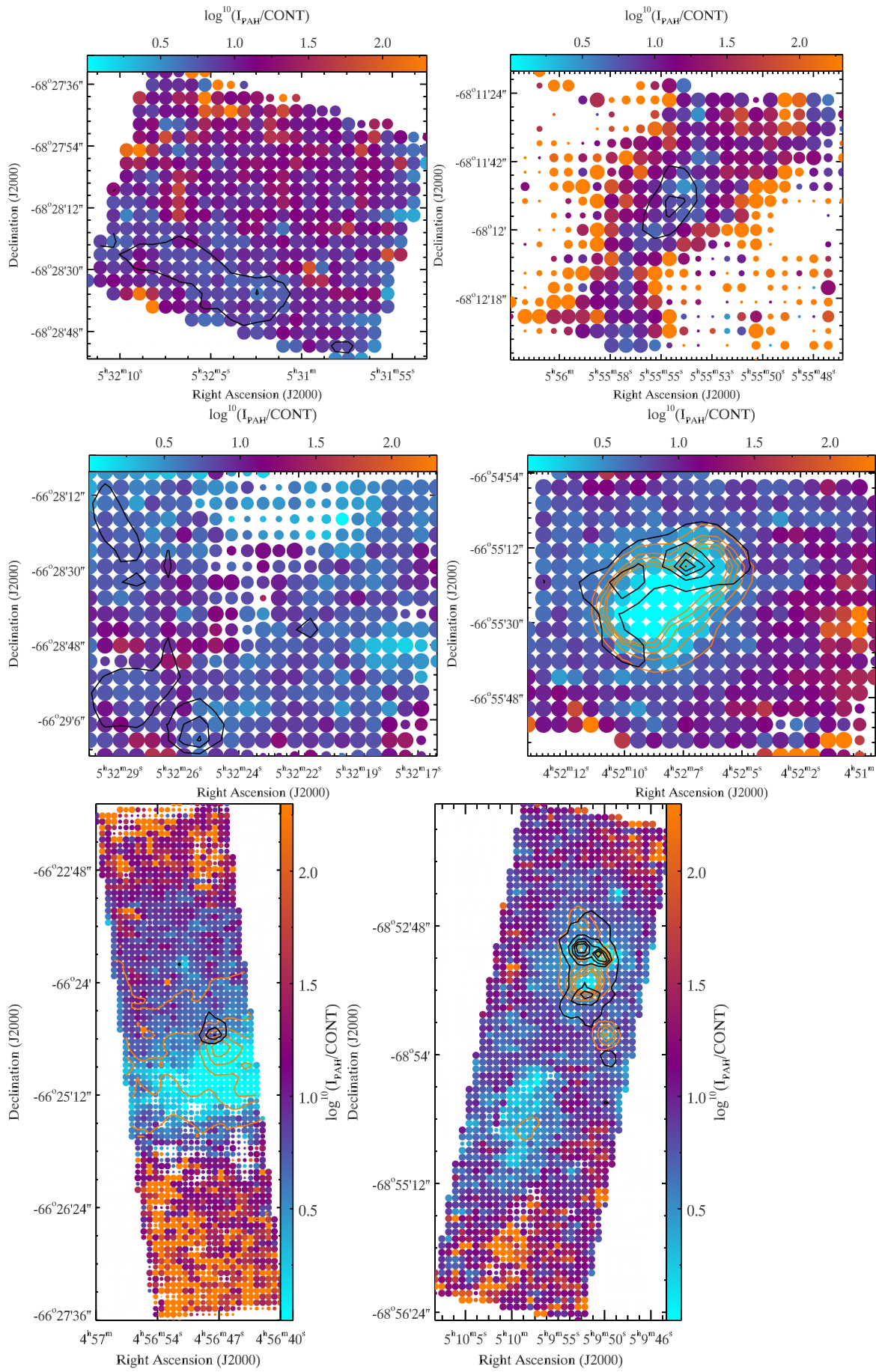


Fig. 5. PAH surface brightness maps of the regions in the LMC. The size of each symbol is a function of the signal to noise (SNR), where the radius of the circle is proportional to SNR for SNR values below 8 and maximal above SNR equal 8.

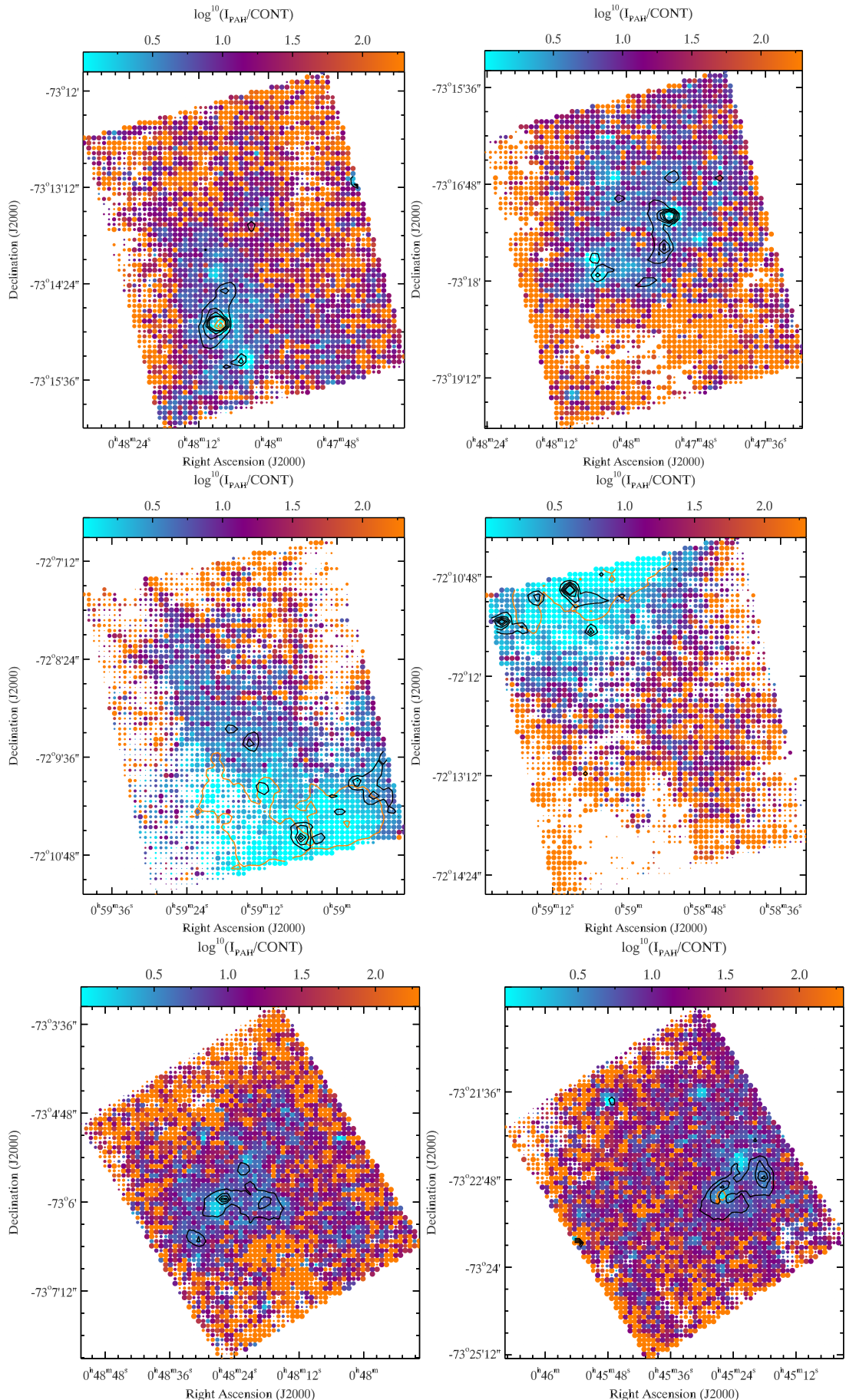


Fig. 6. PAH surface brightness maps of the regions in the SMC. The size of each symbol is a function of the signal to noise (SNR), where the radius of the circle is proportional to SNR for SNR values below 8 and maximal above SNR equal 8.

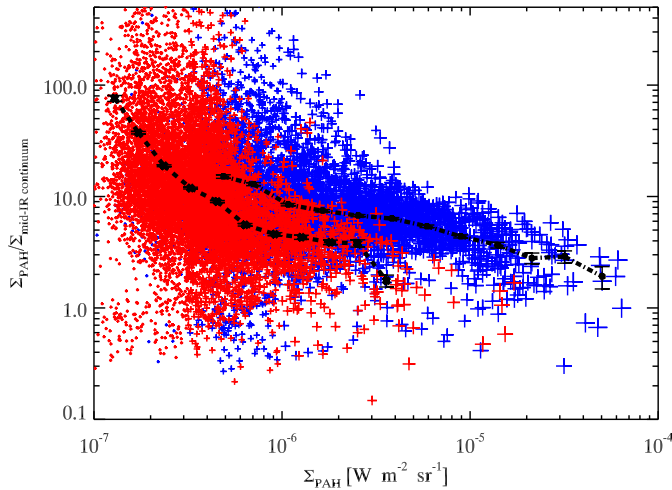


Fig. 7. Scatter diagram of PAH to continuum ratio as a function of the PAH surface brightness. The size of the symbol is proportional to the PAH brightness. Each color corresponds to a different region. Only ratios with a significance above 8 are shown. The thick black crosses show the running median value.

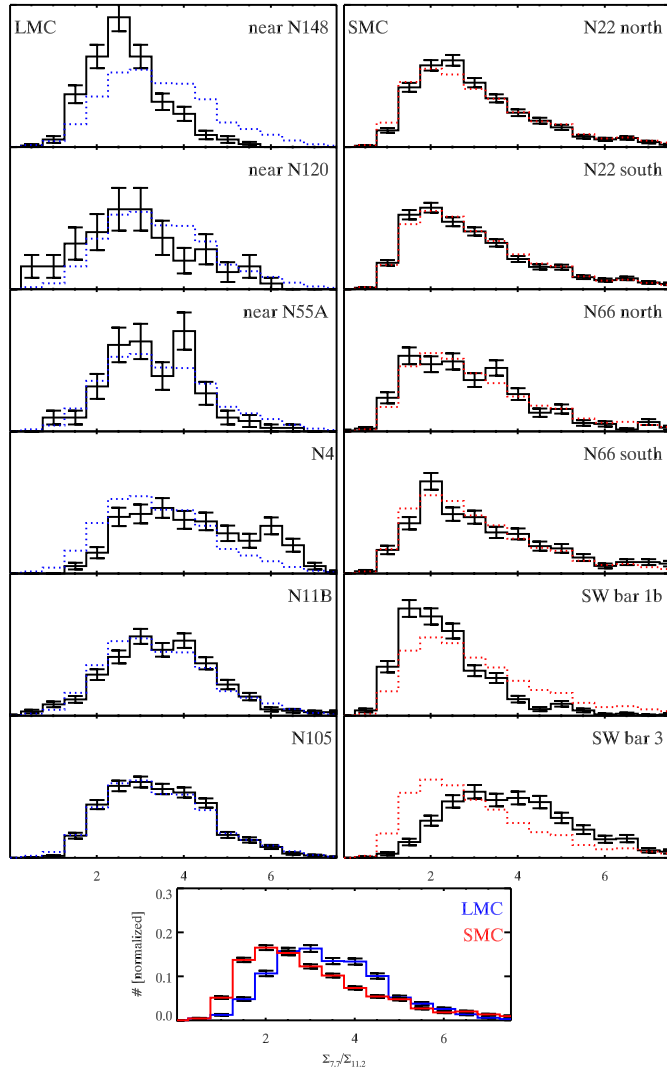


Fig. 8. Histogram of CC-mode emission at 7.7 μm over CH mode emission at 11.2 μm ratio per region.

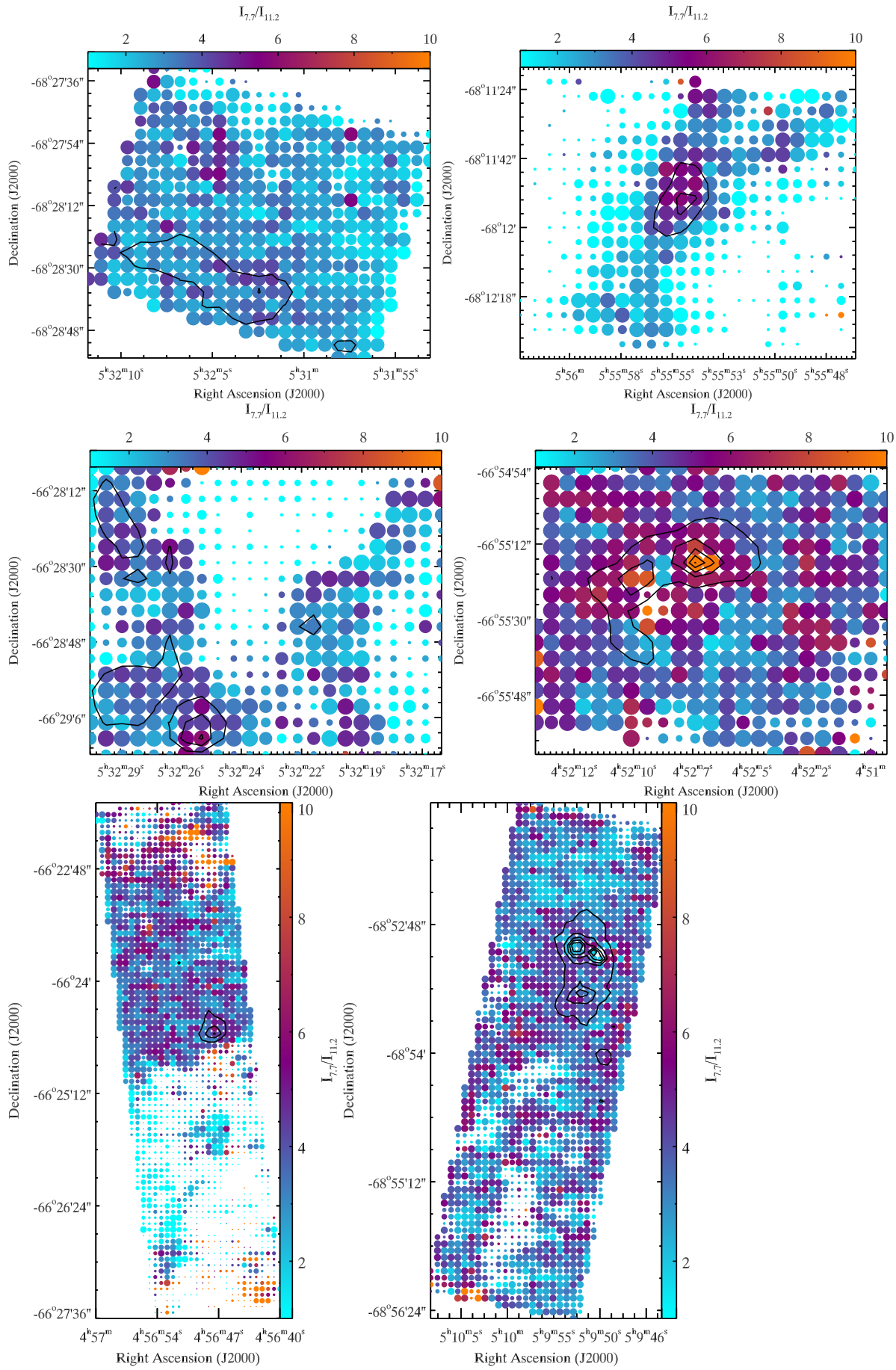


Fig. 9. PAH surface brightness maps of the regions in the LMC. The size of each symbol is a function of the signal to noise (SNR), where the radius of the circle is proportional to SNR for SNR values below 8 and maximal above SNR equal 8.

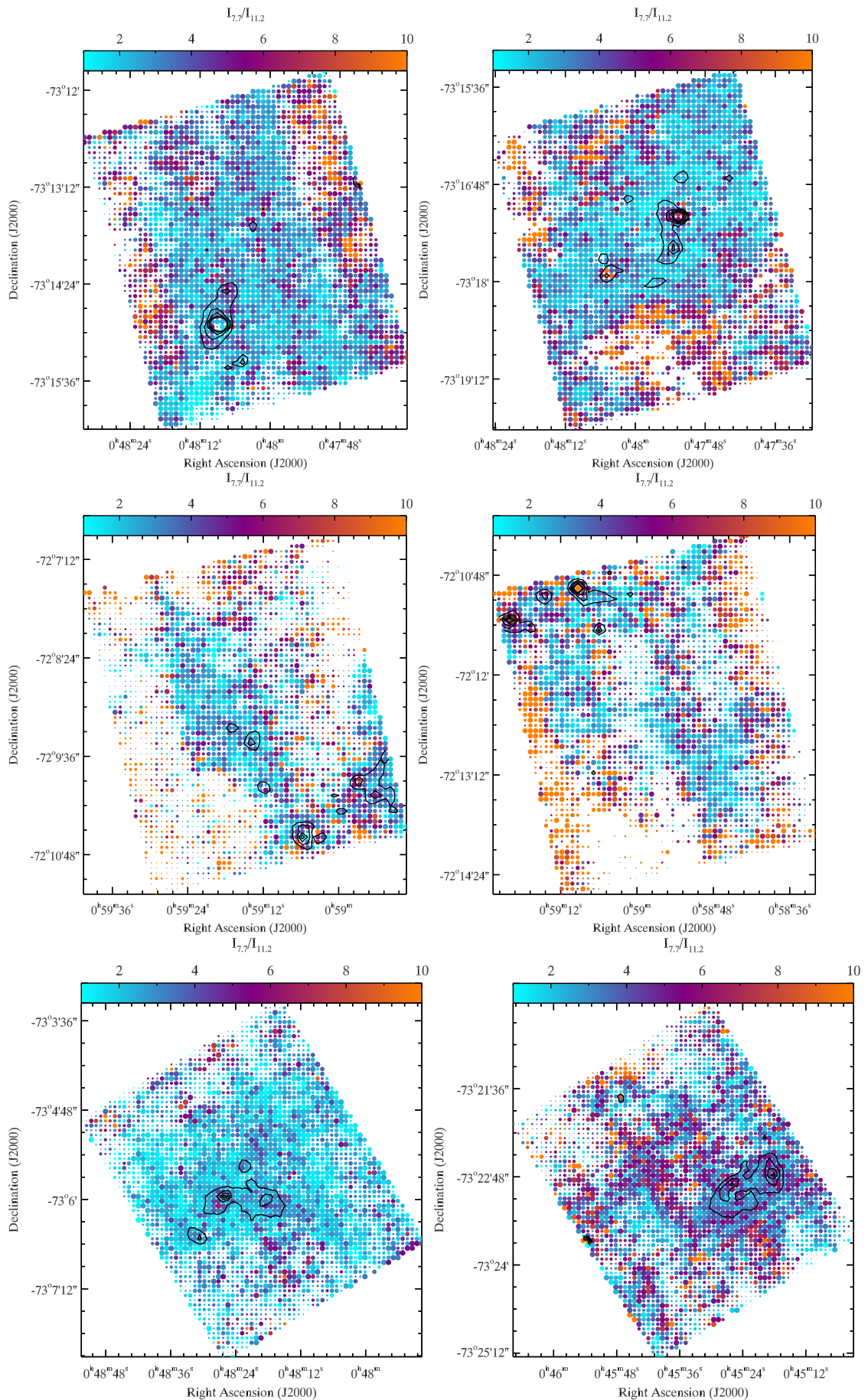


Fig. 10. PAH surface brightness maps of the regions in the SMC. The size of each symbol is a function of the signal to noise (SNR), where the radius of the circle is proportional to SNR for SNR values below 8 and maximal above SNR equal 8.

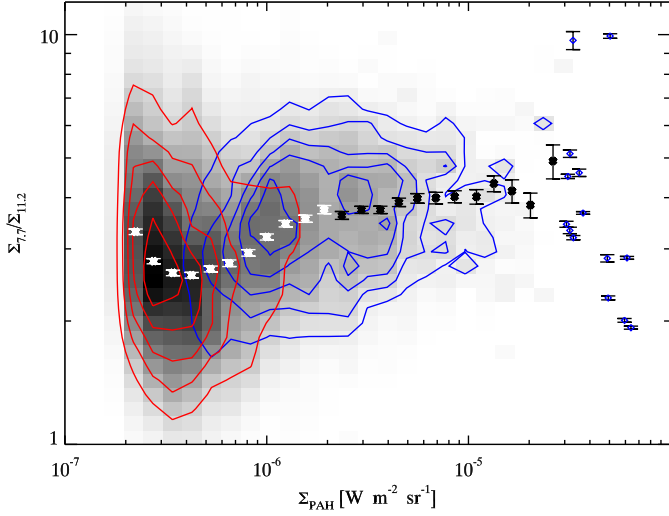


Fig. 11. Scatter diagram of CC-mode emission at $7.7 \mu\text{m}$ over CH mode emission at $11.2 \mu\text{m}$ ratio versus the PAH surface brightness. The thick black crosses show the running median value which shows an interesting behaviour of peaking both at the high and the low end.

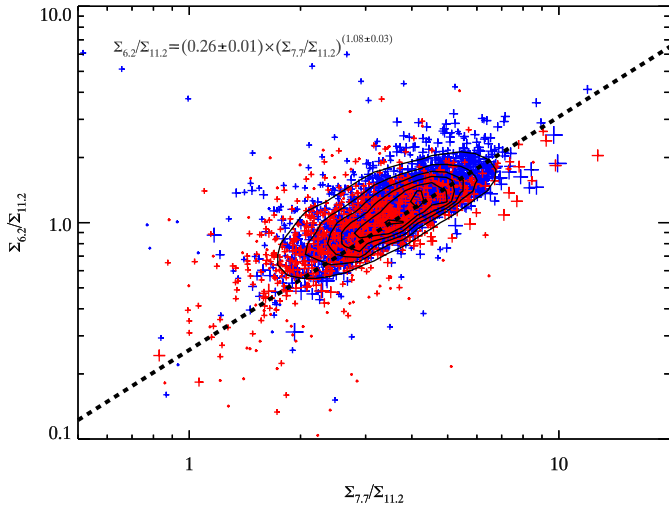


Fig. 12. Scatter diagram of CC-mode emission (6.2 and $7.7 \mu\text{m}$) over CH mode emission at $11.2 \mu\text{m}$ ratio. The size of the points is proportional to the PAH surface brightness. The dashed line corresponds to a powerlaw fit. The correlation is very tight with a near linear interdependence. The few points that are clear outliers correspond to individual l.o.s dominated by an embedded source.

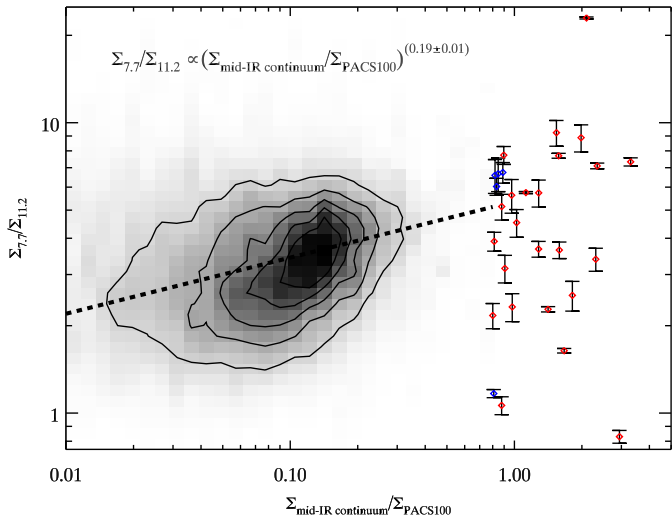
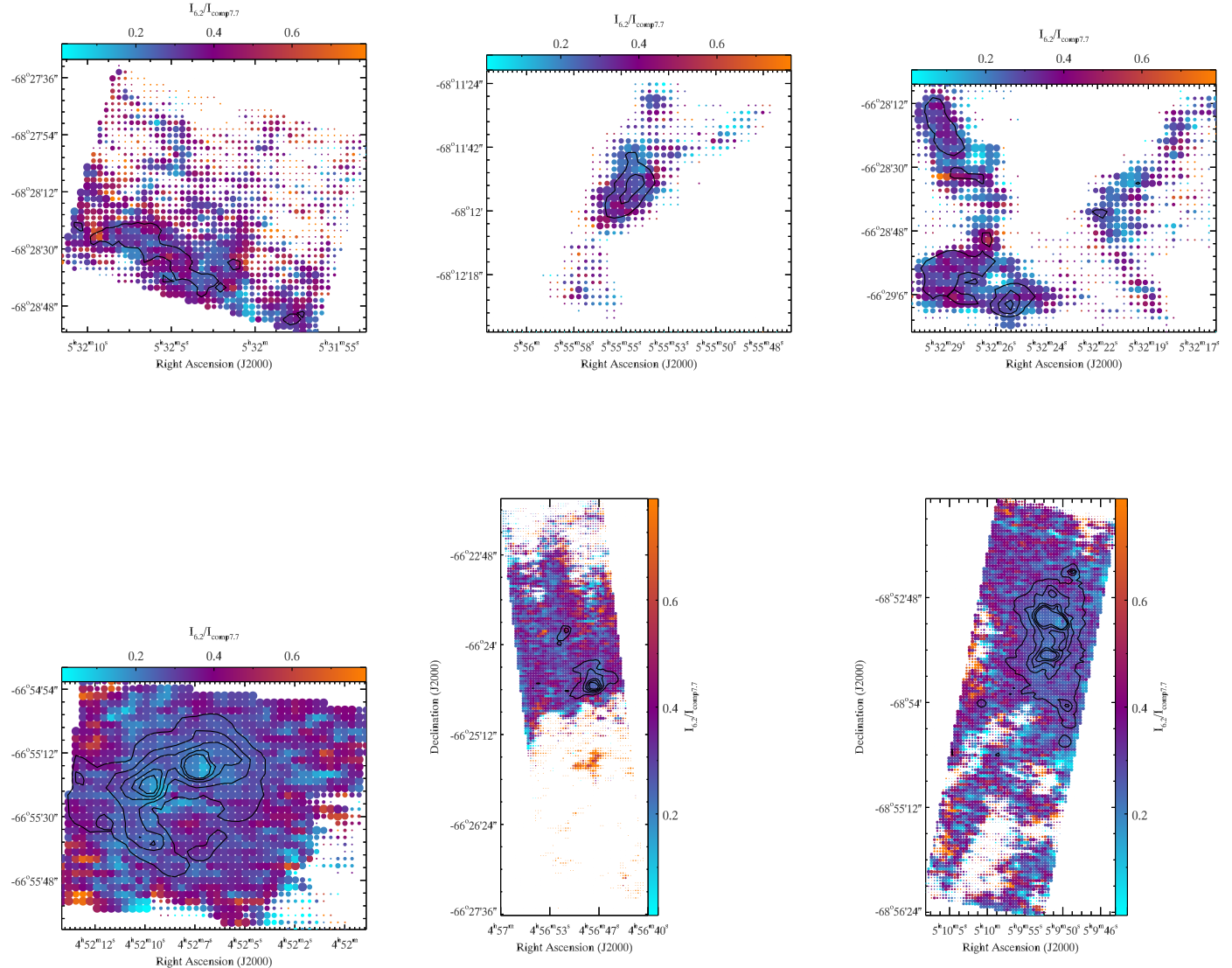


Fig. 13. Scatter diagram of CC-mode emission (6.2 and 7.7 μm) over CH mode emission at 11.2 μm ratio. The size of the points is proportional to the PAH surface brightness. The dashed line corresponds to a powerlaw fit. The correlation is very tight with a near linear interdependence. The few points that are clear outliers correspond to individual l.o.s dominated by an embedded source.


Fig. 14. XXX

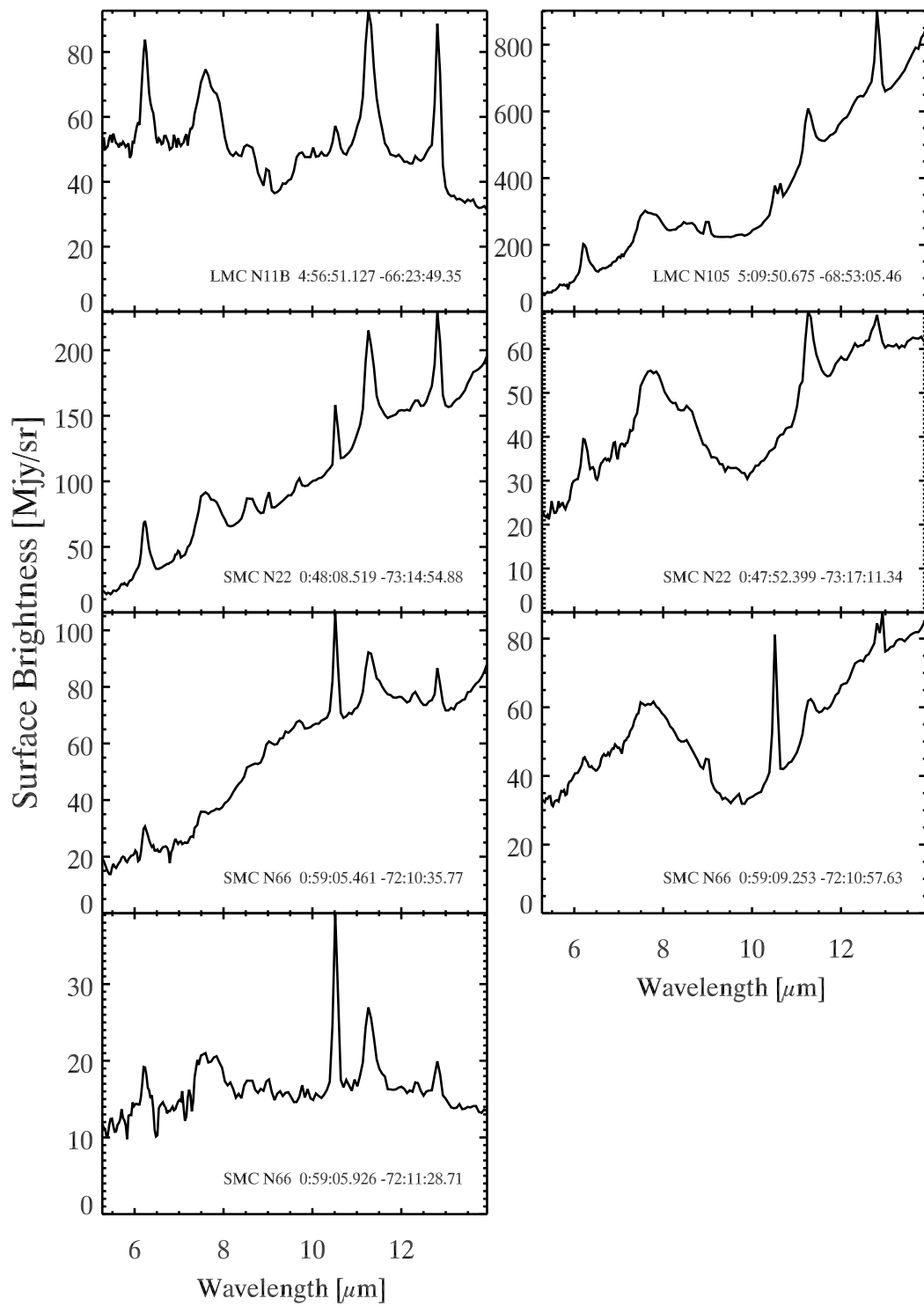


Fig. 15. Spectra of the brightest embedded sources.

The Fitting Method We perform the fit of mid-IR spectra in two parts:

1. Atomic and molecular unresolved line fitting (one by one);
2. Dust continuum, aromatic bands, foreground extinction (dust and ices) and stellar contamination (simultaneous).

Appendix .1: Line Fitting

Central wavelength [μm]	Species and Transition	Input Code Label
5.1286570	H I 6-10	H16-10
5.5111600	H ₂ 0-0 S(7)	H2S7
5.6098000	[Mg v] 3P ² -3P ¹	MgV
5.9082130	Humphreys γ	Huc
5.9810000	[K iv]	KIV
6.1085600	H ₂ 0-0 S(6)	H2S6
6.7090000	[Cl v] 2P ⁰ -2P ⁰	ClV
6.9095200	H ₂ 0-0 S(5)	H2S5
6.9479840	He II 8-9	HeII1
6.9852740	[Ar ii] 2P ^{3/2} -2P ^{1/2}	ArII
7.3178000	[Na iii] 2P ⁰ -2P ⁰	NaIII
7.4598580	Pfund α	Pfa
7.5024930	Humphreys β	Hub
7.6524000	[Ne vi] 2P ⁰ -2P ⁰	NeVI
7.8145000	[Fe sc vii] 3F ³ -3F ⁴	FeVII
7.9015800	[Ar v] 3P ¹ -3P ²	ArV
8.0250500	H ₂ 0-0 S(4)	H2S4
8.7600640	H I 7-10	H17-10
8.9910300	[Ar iii] 3P ² -3P ¹	ArIII1
9.0420000	[Ni vi] 4P ^{5/2} -4F ^{5/2}	NiVI
9.5267000	[Fe viii] 3F ² -3F ³	FeVII
9.6649100	H ₂ 0-0 S(3)	H2S3
9.7134750	He II 9-10	HeII2
10.338500	[Si i] 1P ¹ -1P ²	SiI
10.510500	[S iv] 2P ^{3/2} -2P ^{1/2}	SIV
12.278610	H ₂ 0-0 S(2)	H2S2
12.368527	Humphreys α	Hua
12.813550	[Ne ii] 2P ^{3/2} -2P ^{1/2}	NeII
13.102190	[Ar v] 3P ⁰ -3P ¹	ArV
13.521000	[Mg v] 3P ¹ -3P ⁰	MgV
14.321680	[Ne v] 3P ¹ -3P ²	NeV1
15.555000	[Ne iii] 3P ² -3P ¹	NeIII1
17.034830	H ₂ 0-0 S(1)	H2S1
17.608246	H I 11-18	H111-18
18.712900	[S iii] 3P ² -3P ¹	SIII1
19.061898	H I 7-8	H17-8
21.829100	[Ar iii] 3P ¹ -3P ⁰	ArIII2
24.317500	[Ne v] 3P ⁰ -3P ¹	NeV2
25.890300	[O iv] 2P ^{3/2} -2P ^{1/2}	OIV
28.218830	H ₂ 0-0 S(0)	H2S0
33.481000	[S iii] 3P ¹ -3P ⁰	SIII2
34.815200	[Si ii] 2P ^{3/2} -2P ^{1/2}	SiII
35.349100	[Fe ii] 6D ^{5/2} -6D ^{7/2}	FeII2
36.013500	[Ne iii] 3P ¹ -3P ⁰	NeIII2

Table .1. Atomic and molecular line list.

The line fitting is done on each line separately, since they are unresolved. For each line i (Table .1), we assume a Gauss profile and second order polynomial baseline:

$$F_{\nu}^{\text{line}}(\nu; i) = \frac{I_{\text{line}}(i)}{\sqrt{2\pi}\sigma(i)} \times \exp\left[-\frac{(\nu - \nu_0(i))^2}{2\sigma(i)^2}\right] + \\ a(i) \times \left[1 + b(i)\left(\frac{\nu}{\nu_0(i)} - 1\right) + c(i)\left(\frac{\nu}{\nu_0(i)} - 1\right)^2\right], \quad (2)$$

where the parameters are:

1. The integrated line intensity, $I_{\text{line}}(i)$, which is free to vary;
2. The line central frequency $\nu_0(i)$ (Table .1), which is either fixed or free to vary by $\pm 1/2$ pixel;
3. The line width, $\sigma(i)$, either fixed to the instrumental resolution $\sigma_{\text{inst}}(i)$, or free to vary between $\sigma_{\text{inst}}(i)/2$ and $2\sigma_{\text{inst}}(i)$.
4. The three baseline parameters $a(i)$, $b(i)$, $c(i)$.

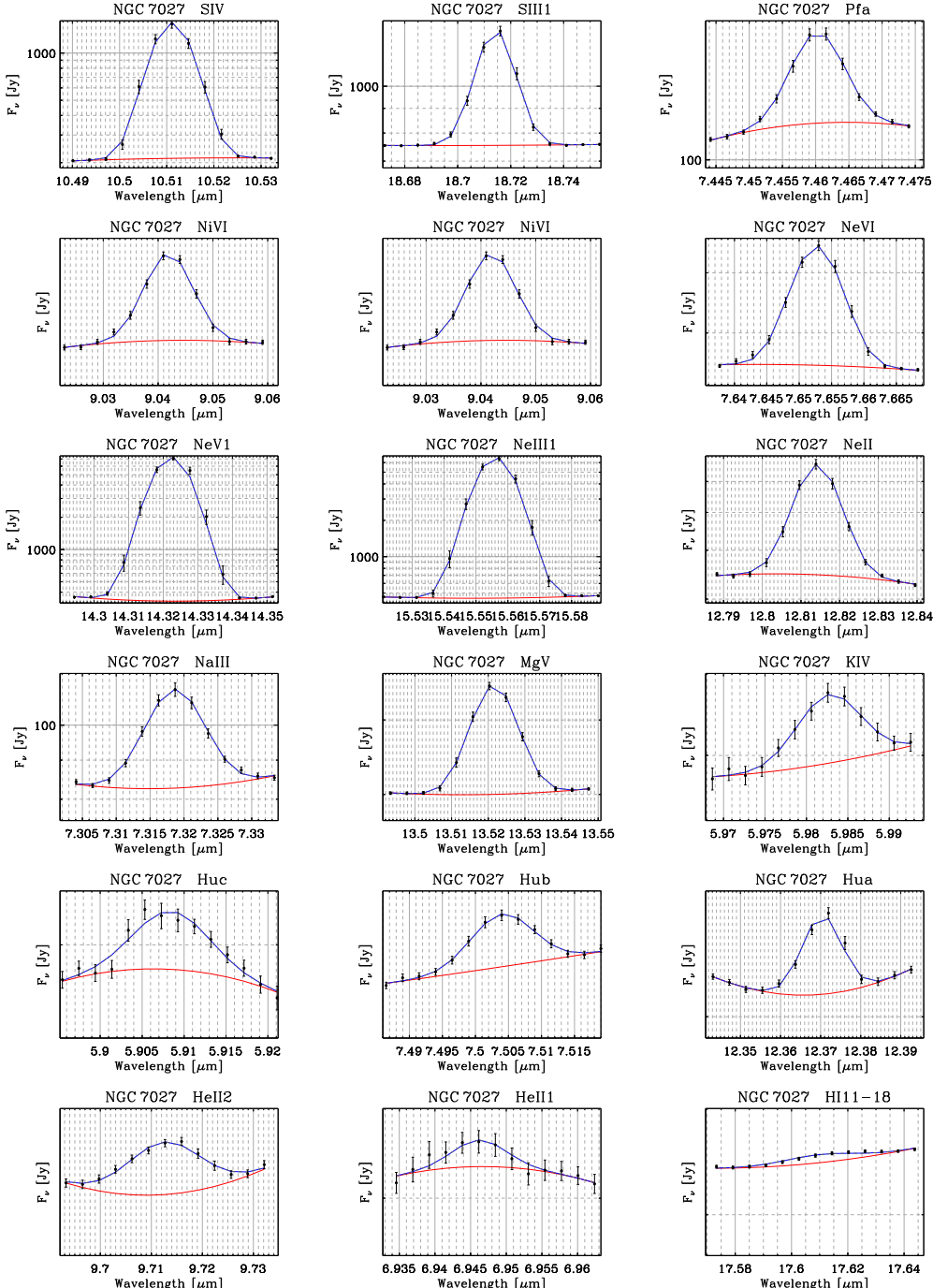


Fig. .1. Select individual line fits of the SWS spectrum of NGC 3467027.

Fig. .1 shows the fits of the lines for the $5-20\mu\text{m}$ SWS spectrum of NGC 3467027 (Bernard Salas et al. 2001). These line templates are then added (fixed) to the other components to fit the total spectrum.

Appendix .2: Continuum and Resolved Feature Fitting

Then the fit of the other components is done simultaneously since they combine in a non-linear way. The components are the followings.

1. The fitted line template (Eq. .2), which is fixed to:

$$F_\nu^{\text{line}}(\nu) = \sum_{i=1}^{N_{\text{line}}} F_\nu^{\text{line}}(\nu; i). \quad (.3)$$

2. The stellar continuum, to account for contamination of old stellar populations or the tail of young stars close to the source, $F_\nu^*(\nu)$. It is modeled by a single burst with PEGASE (Fioc & Rocca-Volmerange 1997), at 5 Gyr. Since we fit only the Rayleigh-Jeans slope ($\lambda \gtrsim 5 \mu\text{m}$), those parameters do not matter. This component is simply scaled up and down. This component is controlled by a single parameter M_* .
3. The dust grain continuum is the linear combination of N_{grain} modified blackbodies, with temperatures $T(i)$ and masses $M(i)$ free to vary, and realistic absorption opacities $Q_{\text{abs}}(\nu; i)$ and specific volume $\rho(i)$ (Table .2):

$$F_\nu^{\text{grain}}(\nu; i) = \frac{M(i)}{d^2} \frac{3}{4\rho(i)} \left(\frac{Q_{\text{abs}}(\nu; i)}{a} \right) B_\nu(T(i); \nu). \quad (.4)$$

Component	Reference	Input Code Label
Graphite	Laor & Draine (1993)	gra
Amorphous carbon (BE)	Rouleau & Martin (1991)	crb
Silicate	Jäger et al. (2003)	sil_norm
Astronomical silicate	Weingartner & Draine (2001)	sil
Corundum	Begemann et al. (1997)	al2o3_compact
Astronomical corundum	Koike et al. (1995)	al2o3_koike

Table .2. Set of grain opacities.

4. The aromatic bands are modeled with asymmetric Lorentz profiles, in order to account for the anharmonicity:

$$F_\nu^{\text{band}}(\nu) = I_{\text{band}}(i) \times \begin{cases} \frac{2}{1 + \Delta\nu_{\text{long}}(i)/\Delta\nu_{\text{short}}(i)} \frac{\Delta\nu_{\text{short}}(i)}{\pi} \frac{1}{(\nu - \nu_0(i))^2 + \Delta\nu_{\text{short}}^2(i)} & \text{for } \nu \geq \nu_0(i) \\ \frac{2}{1 + \Delta\nu_{\text{short}}(i)/\Delta\nu_{\text{long}}(i)} \frac{\Delta\nu_{\text{long}}(i)}{\pi} \frac{1}{(\nu - \nu_0(i))^2 + \Delta\nu_{\text{long}}^2(i)} & \text{for } \nu < \nu_0(i) \end{cases} \quad (.5)$$

For each band, the free parameters are $I_{\text{band}}(i)$, $\nu_0(i)$, $\Delta\nu_{\text{short}}(i)$ and $\Delta\nu_{\text{long}}(i)$. The profile can be fixed, then the only parameter is $I_{\text{band}}(i)$.

5. We assume a foreground slab extinction, with two components: dust and ices. Those component vary independently. The free parameters are the A_V of each component. The wavelength dependent absorption probability is:

$$P_{\text{abs}}(\nu) = \exp \left(-A_V^{\text{dust}} A_{\text{dust}}(\nu) - A_{15.2 \mu\text{m}}^{\text{CO}_2} A_{\text{CO}_2}(\nu) \right), \quad (.6)$$

where $A_{\text{dust}}(nu)$ is the wavelength dependent optical depth of the standard dust composition (silicate, graphite), normalised to A_V , and $A_{CO_2}(\nu)$ is the wavelength dependent optical depth of CO₂ ices (White et al. 2009, at 75 K), normalised at 15.2 μm .

The total model is then fit to the observed spectrum by minimizing the χ^2 . The total mode is:

$$F_\nu^{\text{model}}(\nu) = \left(F_\nu^\star(\nu) + \sum_{i=1}^{N_{\text{grain}}} F_\nu^{\text{grain}}(\nu; i) + \sum_{i=1}^{N_{\text{band}}} F_\nu^{\text{band}}(\nu; i) \right) \times P_{\text{abs}}(\nu) + \sum_{i=1}^{N_{\text{line}}} F_\nu^{\text{line}}(\nu; i). \quad (7)$$

Appendix .3: Calibration of the Aromatic Feature Profiles

We calibrate the PAH feature parameters in the 5 to 20 μm range.

1. To fix the profiles of the aromatic band, we first fit the *ISO/SWS* spectrum of the Red Rectangle, in order to calibrate the narrow bands (Fig. .2). The plateaux of this region are not prominent. Those will be fit in the second step.

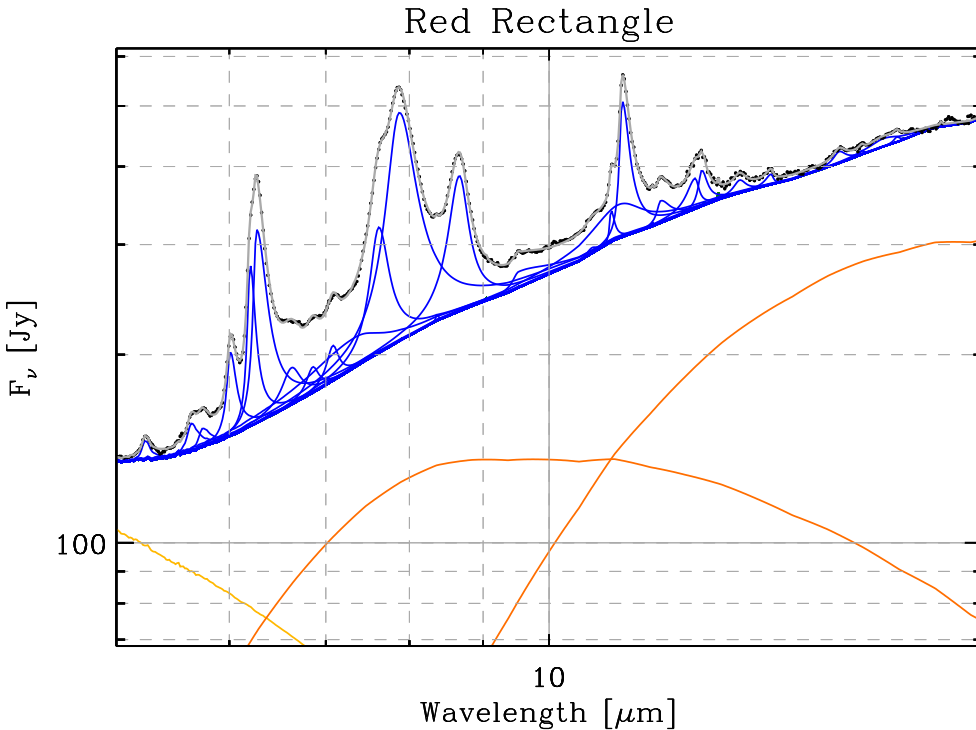


Fig. .2. Calibration of the band profile on the Red Rectangle.

2. Then, the narrow band profile is used as a basis to fit the *ISO/SWS* spectrum of NGC 3467027 (Fig. .3). We derive the plateau of the 8 μm and 12 μm complexes from this fit. The 17 μm complex is too weak to do so.
3. Moreover, the 8.6 μm features is off-centered. Since the sources of the LMC are more of the type of NGC 3467027, we let this feature free to vary and adopt this new profile.
4. Finally the 17 μm complex is fit from the IRS spectrum of M 17 (position 2), taking into account foreground extinction.

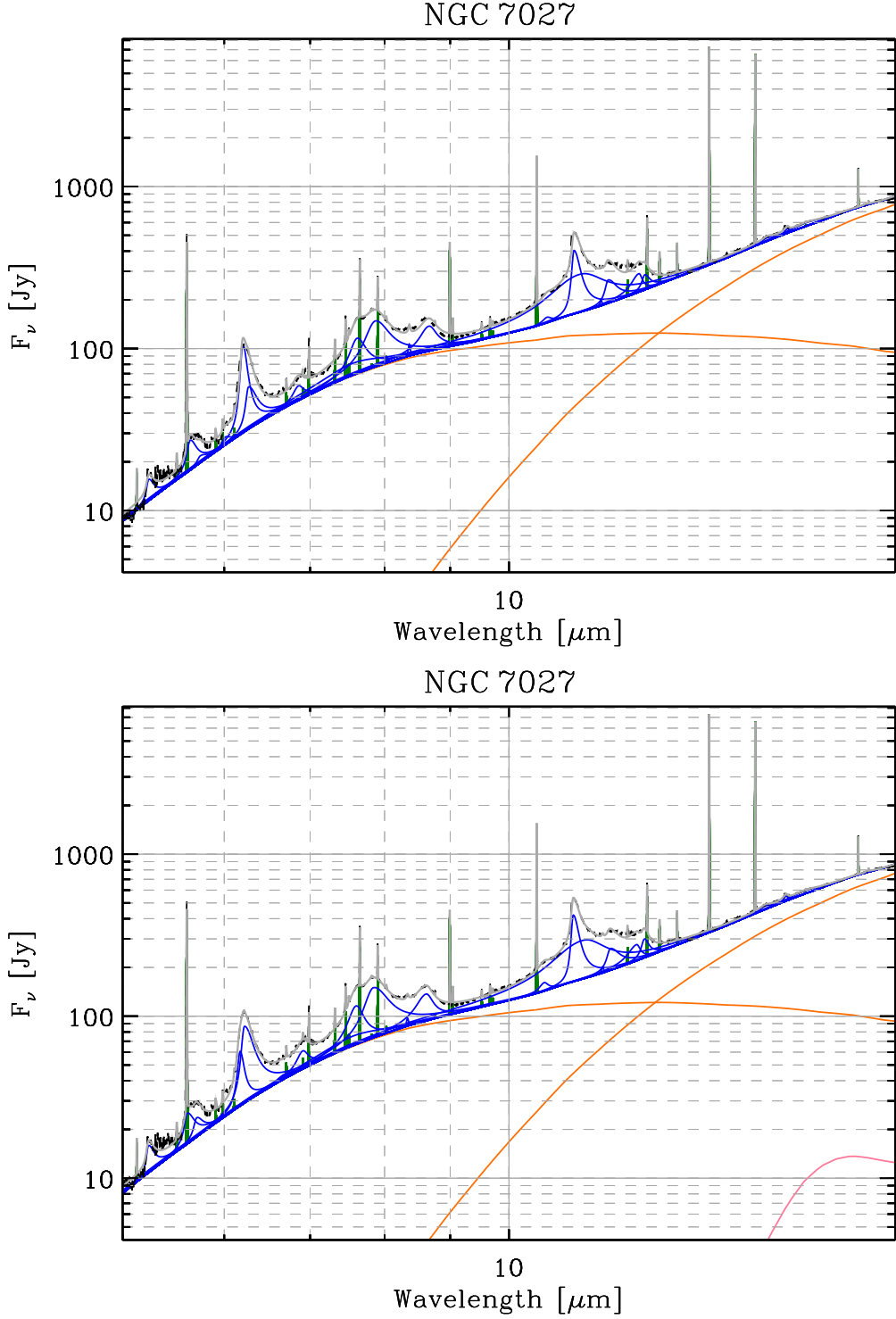


Fig. .3. Calibration of the band profile on NGC 3467027. The top panel shows the fit, fixing the narrow features to the parameters derived from the Red Rectangle. The bottom panel shows the fit letting the widths vary by 10 %.

The final band parameters are shown in Table .3 and on Fig. .7. In Table .3, the parameters refer conveniently to the wavelength, although the band is parametrised by the frequency. The

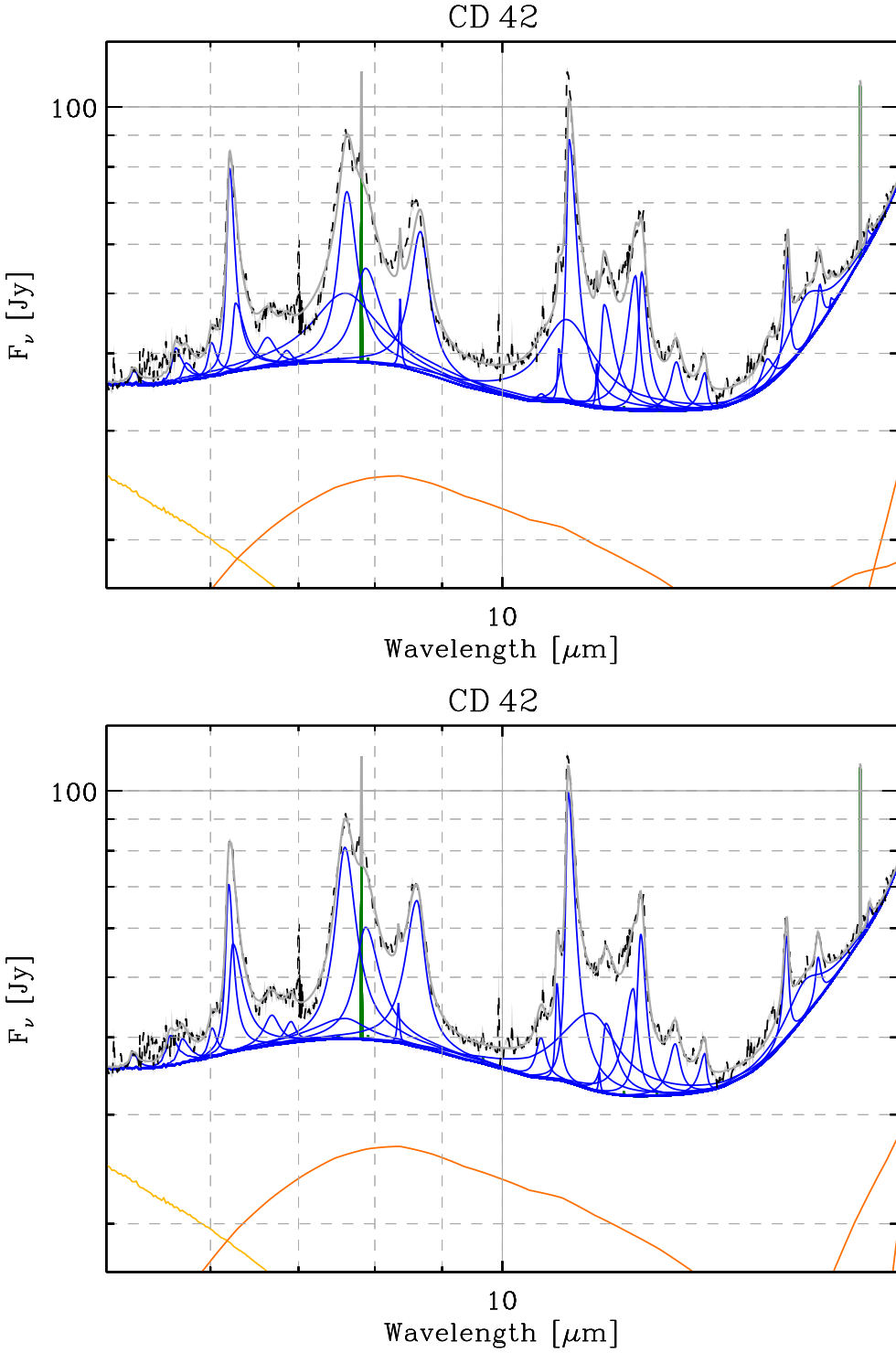
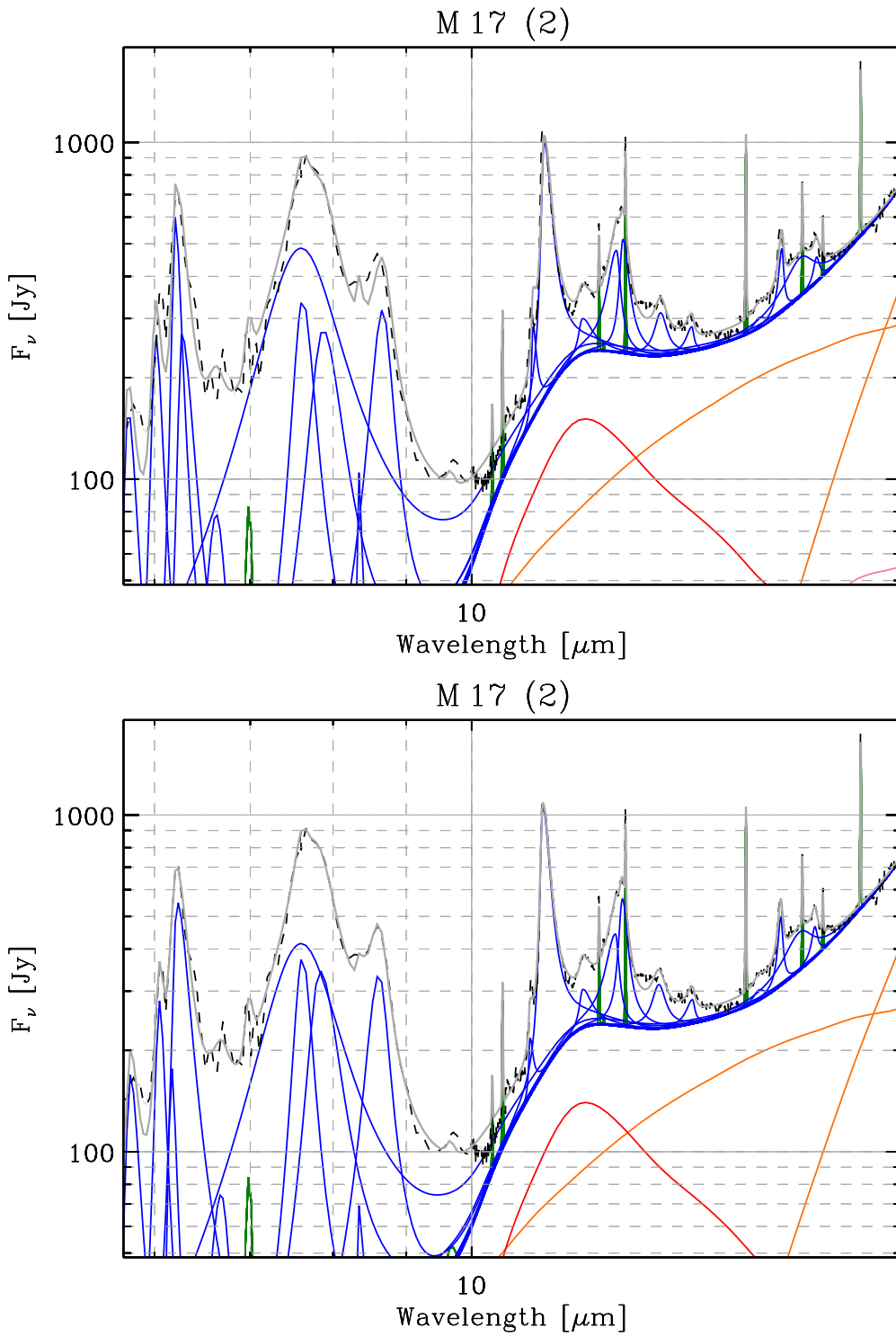


Fig. 4. Calibration of the band profile on CD 42. The top panel shows the fit, fixing the narrow features to the parameters derived from the Red Rectangle. The bottom panel shows the fit letting the widths vary by 10 %.

transformation is the following:

$$\left\{ \begin{array}{l} v_0 = \frac{c}{\lambda_0} \\ \Delta v_{\text{short}} = \frac{c}{\lambda_0 - \Delta \lambda_{\text{short}}} - \frac{c}{\lambda_0} \\ \Delta v_{\text{long}} = \frac{c}{\lambda_0} - \frac{c}{\lambda_0 + \Delta \lambda_{\text{long}}} \end{array} \right. \quad (8)$$



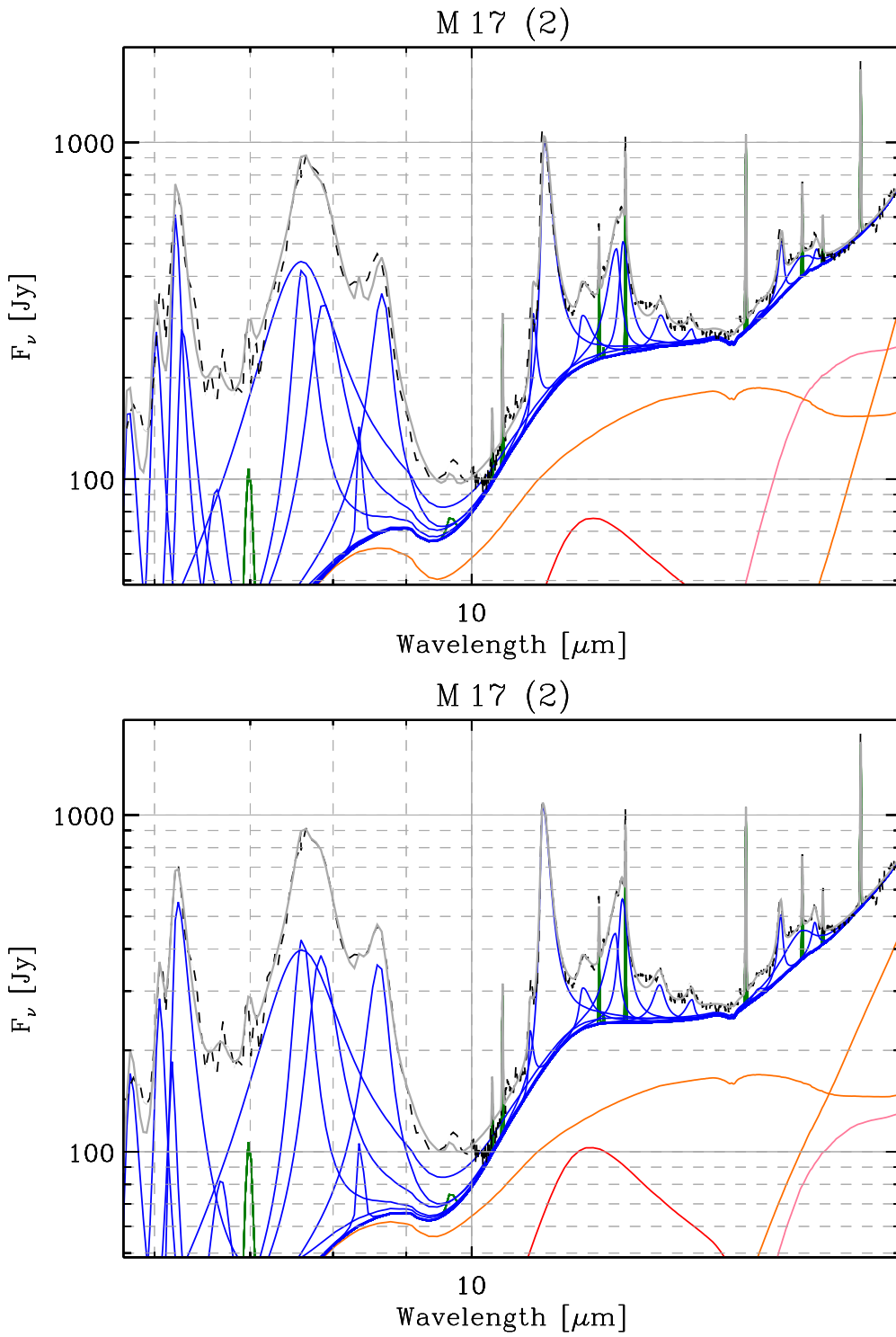
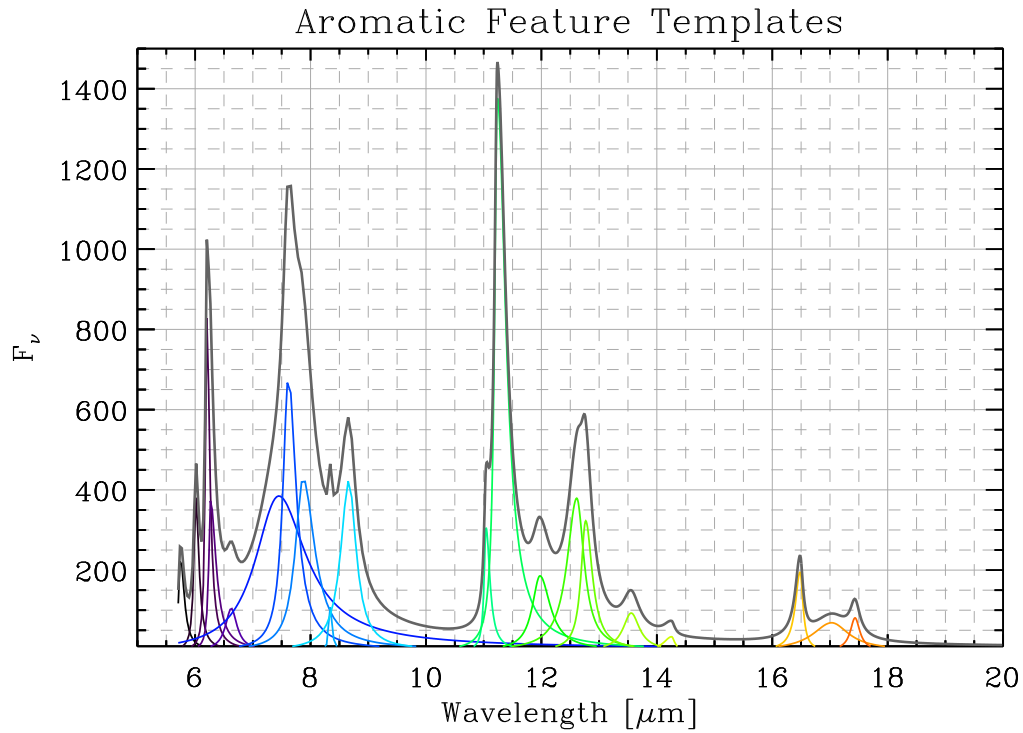


Fig. .6. Calibration of the band profile on M 17, with a corundum component. The top panel shows the fit, fixing the narrow features to the parameters derived from the Red Rectangle. The bottom panel shows the fit letting the widths vary by 10 %.

**Fig. 7.** Calibrated aromatic feature profiles.

λ_0 [μm]	$\Delta\lambda_{short}$ [μm]	$\Delta\lambda_{long}$ [μm]	Input Code Label
5.2395	0.0252	0.0583	Small 5.2
5.6437	0.0400	0.0800	Small 5.7 (1)
5.7490	0.0400	0.0800	Small 5.7 (2)
6.0107	0.0400	0.0666	Small 6.0
6.2034	0.0313	0.0600	Main 6.2 (1)
6.2673	0.0369	0.1163	Main 6.2 (2)
6.6274	0.1200	0.1200	Small 6.6
6.8549	0.0800	0.0800	Small 6.8
7.0792	0.0800	0.0800	Small 7.1
7.6000	0.4800	0.5025	Plateau 7.7
7.6171	0.1186	0.1453	Main 7.7 (1)
7.8705	0.1700	0.2452	Main 7.7 (2)
8.3624	0.0163	0.0163	Small 8.3
8.6205	0.1834	0.1334	Main 8.6
9.5245	0.1077	0.6000	Small 9.5
10.7071	0.1000	0.1000	Small 10.7
11.0383	0.0270	0.0731	Small 11.0
11.2379	0.0535	0.1525	Main 11.2
11.4004	0.7200	0.6366	Plateau 11.3
11.7964	0.0208	0.0208	Small 11.8
11.9497	0.0804	0.2219	Small 11.9
12.6268	0.2000	0.0944	Main 12.7 (1)
12.7603	0.0804	0.1400	Main 12.7 (2)
13.5593	0.1595	0.1605	Small 13.6
14.2571	0.1521	0.0590	Small 14.2
15.8931	0.1786	0.2000	Small 15.6
16.4829	0.1000	0.0585	Small 16.4
17.0829	0.4978	0.5612	Plateau 17.0
17.4285	0.1000	0.1000	Small 17.4
17.7711	0.0308	0.0752	Small 17.8
18.9256	0.0346	0.1157	Small 18.9

Table 3. Calibrated aromatic band parameters.